Atomistic mechanisms of crack nucleation and propagation in amorphous silica

Tengyuan Hao and Zubaer M. Hossain[*]

*Laboratory of Mechanics & Physics of Heterogeneous Materials Department of Mechanical Engineering
and University of Delaware, Newark, Delaware 19716, USA*

This paper presents an atomistic understanding of the nanoscale processes that govern crack nucleation and propagation in amorphous silica using a combination of theoretical calculations and molecular dynamics simulations with the ReaxFF potential. We show that both crack nucleation and propagation are governed by chainlike nanoscale virial stress-fibers formed by an intricate mixture of Si and O atoms. The stress-fibers are of a few nanometers in length, aligned parallel to the loading direction, and spatially localized at the evolving crack front at the nucleating site or a propagating crack tip. They form and break continuously during the crack nucleation and propagation process and are responsible for localizing stress at the crack nucleation site or propagating crack front. As soon as the stress-fibers reach a critical density the material starts nucleating cracks or leads to the propagation of initial crack. Additionally, the virial stress fields in the domain is highly heterogeneous and species-dependent—and the O and Si atoms play fundamentally distinct roles throughout the deformation process. With increased loading, heterogeneity in virial stress for the Si atoms goes up, whereas for the O atoms it goes down. Furthermore, from the virial and Hardy estimates of atomic stress, it is found that the stress field emanating from the crack tip decays as $1/r$. Also, presence of holes or pores within the interaction distance of a crack tip intensifies the stress state of the stress-fibers near the crack front leading to an improved effective toughness compared to the situation where the pore is far from the crack tip. Nucleation and propagation of cracks are strictly mediated by a complex admixture of localized bond rupture processes across a set of interacting stress-fibers. The details of the atomistic process regulating the underlying mechanisms are undetectable from the macroscopic stress-strain data.

I. INTRODUCTION

Silica is a widely used material with versatile applications in microelectronics [1], photonics [2], sensing [3,4], ultrastrong nanowires [5], chromatography [6], pharmaceuticals [7], and structural materials [8,9]. In spite of decades long research and multifarious technological applications of silica (whose projected global market is expected to increase to $14.27 billion in 2019 from $9.26 billion in 2014), its structural and mechanical behavior continues to puzzle scientists and engineers [10–16]. Despite the widely observed phenomena that silica fractures in a brittle manner, the fundamental atomistic mechanisms that govern fracture in silica remain less understood [9,13,17–19]. In addition to a needed fundamental understanding of how does crack nucleate and propagate in an amorphous or inhomogeneous media at the nanoscale, the rapid emergence of flexible electronics demands a thorough understanding of the nanoscale conditions that define the initiation of failure or irreversible deformation in amorphous silica.

The key difficulty in elucidating the crack nucleation and propagation mechanisms in amorphous silica arises from its highly inhomogeneous elastic behavior [13] and the amorphous character of the underlying atomic structure [14]. Although there has been tremendous developments in understanding the atomic structures of silica, it remains unknown how the individual species (Si and O) respond to applied deformation and how do they distribute deformational energy or carry applied deformation at finite temperatures, particularly in the nonlinear regime of mechanical deformation. At the macroscopic scale, it is known that mechanical properties of amorphous silicates are sensitive to structural transformations mediated by deformation and pressure. At high pressure, amorphous silica exhibits an order of magnitudes reduction in strength due to transformation of its fourfold coordination to sixfold coordination [20,21]. Also, structural rearrangement of silica rings has been shown to induce anisotropy and non-Newtonian behavior [22] governed by the topography of enthalpy disorder [23–27]. Furthermore, a number of investigations have been performed in assessing silica structure under a variety of processing conditions including cooling rate, melting temperature, and annealing rate. There is a qualitative consensus among the findings of these investigations that structural configurations of amorphous silica are independent of the processing condition, highlighting the prevalence and retainment of tetrahedral networks in silica [28,29]. While these studies provide critical information on atomic scale structure of silica under undeformed conditions, there is a knowledge gap in understanding how the constituents of the tetrahedra respond to finite deformation and form the basis for strength and toughness reduction in presence of a nanocrack, an edge, or a nanopore.

[*]zubaer@udel.edu

In the context of mechanical properties, a wide body of literature is focused on determining the macroscopic stress-strain behavior of amorphous silica [27–41]. They reveal the implications of cooling rate, melting temperature, and strain rate on atomic scale structure and macroscopic mechanical properties such as stiffness and strength. It is found that both stiffness and strength can be strain-rate dependent, whereas fracture strain is independent of the strain rate, and strength is found to depend weakly on the cooling rate [31,39,42]. Regardless of the deformation intensity, the material maintains the SiO$_4$ tetrahedra, and the bond angle between Si-O-Si triplets changes during deformation. Furthermore, topological heterogeneity has been proposed to cause nanoductility in silicate glasses [43]. While these studies provide useful information on the material behavior of amorphous silica, species-dependent atomistic mechanisms governing nucleation or propagation of nanocracks remain less understood. Because of the intricate nature of the atomic structure and long-range structural correlations formed by its sustained tetrahedral units at finite deformation and temperatures, understanding the condition of fracture in silica is a nontrivial task particularly with the available theoretical resources that are mostly developed for homogeneous solids at the continuum scale [44–46]. While the physics of mechanical deformation under extreme conditions in amorphous materials are very different from crystalline solids, existing explanations on the deformation mechanisms rely on continuum scale theories that are designed to describe mostly isotropic materials and the role of atomistic disorder remains largely ignored in describing the underling physics. As a result, there is a limited understanding of the atomistic processes that form the basis for effective toughness and strength in amorphous solids.

Toughness and strength are a set of mechanical properties that govern the robustness of the material and their correlation with nanoscale structural features remain underdeveloped. The ideal strength in defect free material is characterized by the maximum stress and toughness is the defined as the highest elastic energy density that a solid can sustain prior to the onset of propagation. There can be two types of toughness [47]: nucleation toughness and fracture toughness. Nucleation toughness of a brittle solid can be obtained by integrating the area under the stress-strain curve, $\Pi_c = \int_0^{\epsilon_f} \sigma d\epsilon$, where ϵ_f is the fracture strain. Fracture toughness is defined by the ability of a material to resist the propagation of a pre-existing crack. It is characterized by the critical energy release rate (denoted by G_c) introduced by Griffith in 1921 [46], or the critical stress-intensity factor (denoted by K_{IC} introduced by Irwin in 1957 [45], or the critical driving force (denoted by the J integral) introduced by Rice [44].

Despite the success in defining toughness in homogeneous materials, its notion and relation with microscopic variables remain elusive for amorphous materials. Under the linear elastic fracture mechanics (LEFM) treatment, the foundation for the equivalence of these definitions is built upon the understanding that the stresses in the vicinity of the tip exhibit an inverse square-root dependence on the distance (r) from the crack tip: $\sigma_{ij} = \frac{K_I}{(2\pi r)^{1/2}} f_{ij}(\theta)$, where, σ_{ij} is local stress, K_I is stress intensity, and $f_{ij}(\theta)$ is a geometric function. Complexity arises when the material is heterogeneous, wherein square-root singularity ceases to hold. For example, a crack propagating from a compliant material to a stiff material exhibits weak singularity: $\sigma_{ij} \propto r^0$; whereas, in propagating in the opposite direction it exhibits stronger singularity: $\sigma_{ij} \propto r^{-1}$ [48–54]. Furthermore, along a bimaterial interface the singularity becomes complex, and stresses show logarithmic dependence: $\sigma \propto r^{-\lambda} \cos(b \ln r)$ with $0 \leqslant \lambda \leqslant -1$ [48]. Nevertheless, there is no information on how a singularity plays out in amorphous material.

Here we investigate the stress fields and atomistic processes that govern failure of amorphous silica with or without an initial crack. Our aim is to understand: (i) the atomistic mechanisms that regulate the condition for nucleation of nanocracks in silica; (ii) determine the role of O and Si atoms on the condition of crack nucleation; (iii) explore the atomistic principles that regulate the propagation of an initial crack; (iv) obtain a measure of stress singularity at the crack tip; and (v) determine how the interaction of stress fields emanating from the crack tip and pore edge affects the fracture criteria in an amorphous material setting. In the following sections, we first describe the computational procedure to model the mechanical behavior of silica, and then we discuss the atomic scale mechanisms that regulate the condition for nucleation and propagation of nanocrack.

II. COMPUTATIONAL APPROACH

While first-principles based methods such as the density functional theory (DFT) are the most reliable ones to study the behavior of a system of interacting atoms, it is computationally unfeasible to apply DFT for large systems containing thousands of atoms containing finite cracks. Among the alternatives, interatomic potential based molecular dynamics (MD) simulations produce reliable outcomes, and there are a number of interatomic potentials available including BKS [55], ReaxFF [56]. The ReaxFF potential has been widely used for a number of studies related to crystalline and amorphous silica as well as silicates [27–29,39–41,57–60]—it has been demonstrated that ReaxFF produces experimentally consistent disordered structure, elastic properties, and dynamics of supercooled liquid.

The MD simulations are carried out using LAMMPS [61]. To create an amorphous configuration of silica from its crystalline phase, we first relax initial atomic structure using the conjugate gradient relaxation scheme with a force tolerance of 1.0×10^{-10} Kcal mole^{-1} Å^{-1}, and then follow three thermodynamic steps that involve: (i) raising the temperature of the statically relaxed domain to 8000 K at constant volume and holding it for 100 picoseconds, (ii) annealing the system from 8000 to 1 K at a cooling rate of 5.0 K/ps at constant volume, and (iii) relaxing the system under the microcanonical ensemble for 50 picoseconds. At the end of the three thermodynamic steps, the system reaches a steady-state thermodynamic condition. The system is then dynamically relaxed to zero pressure and 300 K temperature following the NPT thermodynamic ensemble. This step removes any residual stress in the domain and prepares the target at the desired room temperature. The cooling rate chosen here is reasonable enough to obtain a realistic description of glass structure [28,40,41,62,63]. The density of the amorphous target is found to be 2.19 g/cc^3, which matches well with the reported computational values

of 2.18–2.22 g/cc³ [28,32,39,64] from atomistic simulations as well as with the experimental value of 2.22 g/cc³ [65]. We choose 0.25 fs as the time step for all the three thermodynamic steps. In the literature a number of values of time step, ranging from 0.5 to 1.6 fs [39,60,62,66], have been used for making amorphous silica and studying its deformation behavior. For our study we found 0.5 fs to obtain converged stress-strain behavior throughout the entire deformation history of the domain covering both the linear and nonlinear regimes of mechanical deformation (including the fracture process).

To model uniaxial stress deformation, uniform displacement $y(t + \Delta t) = y(t)(1 + \dot{\epsilon}_{yy} \times \Delta t)$ is applied over the entire domain along the y direction with a strain rate of $\dot{\epsilon}_{yy} = 1.0 \times 10^{-6}$ fs^{-1}. Using the aforementioned setup, the elastic properties of silica is calculated from the stress-strain data, which are obtained directly from the MD simulations through tensorial description of system pressure. For uniaxial loading along the y direction, the macroscopic stress-strain data (obtained directly from the MD simulations) are fitted to a fourth-order polynomial:

$$\sigma_{yy} = \beta_1 \epsilon_{yy} + \beta_2 \epsilon_{yy}^2 + \beta_3 \epsilon_{yy}^3 + \beta_4 \epsilon_{yy}^4, \qquad (1)$$

where β_i's are the elastic moduli of different orders and they are calculated by fitting this fourth-order polynomial to the stress-strain data and differentiating the polynomial with respect to strain and evaluating the expression at $\epsilon_{yy} = 0$. The strength is calculated from the maximum of the stress-strain curve, the crack-nucleation toughness is calculated by integrating the area under the stress-strain curve, and the fracture toughness is computed from the stress-intensity factor and the J-integral. To examine the mechanical behavior of the individual atoms during the deformation and fracture processes, we use the virial stresses of the atoms, and for exploring the continuum scale features (such as the fracture toughness) and effective behavior of the oxygen and silicon atoms in the domain we employ the Hardly stress framework. The details of stress calculation are described in later sections.

III. RESULTS AND DISCUSSION

Our results and discussions are divided into two main sections. First we describe the atomistic processes that govern crack nucleation, and then we explain the propagation behavior of an initial crack in the domain.

A. Constitutive behavior of amorphous silica

The condition for crack nucleation is investigated from the uniaxial stress response of SiO$_2$, obtained by applying uniaxial stress to the domain and allowing relaxation along the lateral directions due to the Poisson's contraction. The deformation simulations are conducted under the NPT thermodynamic condition. The loading is applied along the y direction and the domain is allowed to relax along the x and z directions. For our investigation on crack nucleation we considered a domain of dimension $46.88 \times 33.79 \times 2.65$ nm³ containing 345 000 atoms. The domain considered for the
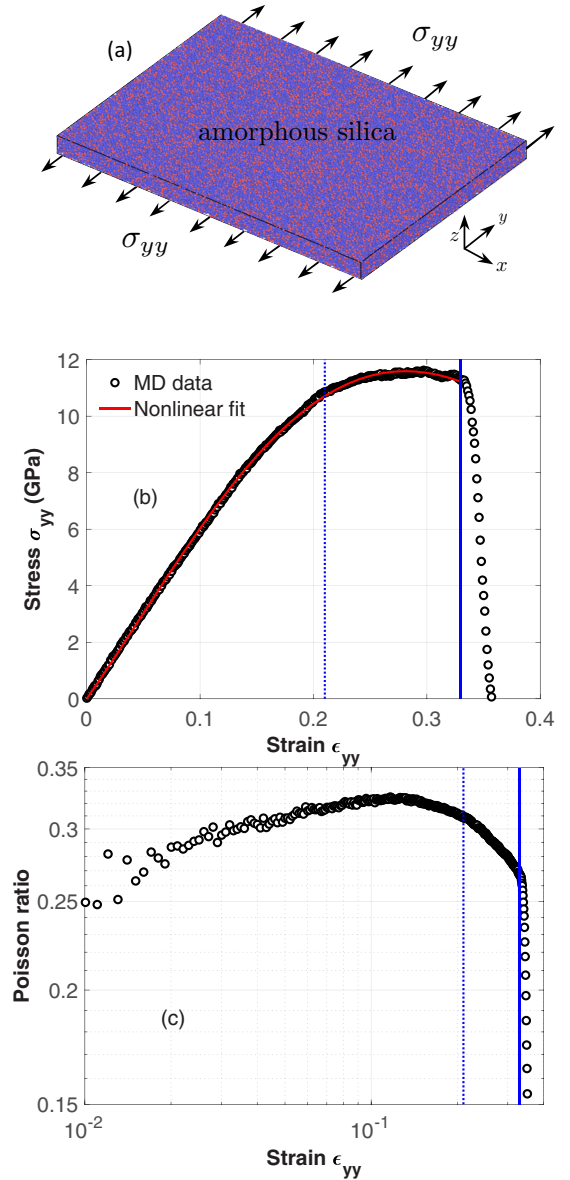
FIG. 1. (a) Amorphous silica domain subjected to a uniaxial stress loading along the y direction. (b) Stress-strain response of the domain. (c) The Poisson's ratio of the domain at different strain states. The vertical dashed line drawn at $\epsilon = 0.21$ indicates the activation of stress saturation, and the vertical solid line drawn at $\epsilon = 0.325$ indicates onset of catastrophic material separation.

study is displayed in Fig. 1, along with its stress-strain response and Poisson's ratio over the entire deformation history.

The Poisson's ratio is calculated from $\nu = -\epsilon_{xx}/\epsilon_{yy}$, where ϵ_{yy} is the applied strain along the loading direction and ϵ_{xx} is the strain along the lateral direction. In the low-deformation regime, $0.0 \leqslant \epsilon_{yy} \leqslant 0.15$, silica shows small monotonous increase in its Poisson's ratio from 0.25 to 0.32; for $0.15 \leqslant \epsilon_{yy} \leqslant 0.21$ it starts to continuously decrease its magnitude; and for $0.21 \leqslant \epsilon_{yy} \leqslant 0.325$, the Poisson's contraction reduces from 0.32 to 0.25. For $\epsilon_{yy} \geqslant 0.325$, the domain undergoes drastic reduction in Poisson's ratio and experience material separation in a few loading steps. Moreover, from the
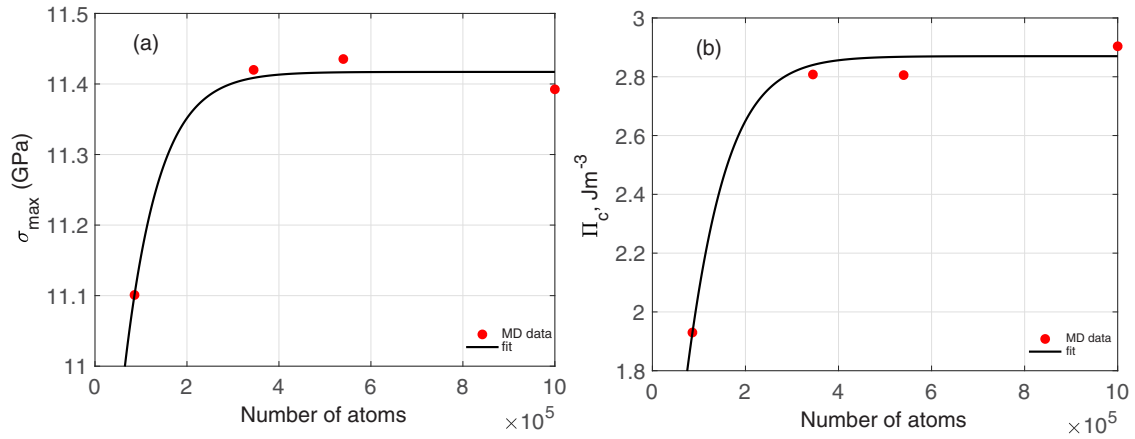
FIG. 2. Effect of domain-size on (a) ideal strength and (b) nucleation toughness in amorphous silica at 300 K.

stress-strain curve, it is seen that the domain shows a linear correlation between stress and strain up to a strain level of 15%. Beyond this strain the domain starts exhibiting nonlinear stress-strain response up to 32.5% strain, followed by a 2% strain window within which nanocracks form and evolve rapidly to separate the domain. To quantify the elastic moduli, we fit the stress-strain relationship presented by Eq. (1) to the MD-generated stress-strain data shown in Fig. 1, and obtain the Young's modulus as 69.1 GPa and the higher-order moduli as $\beta_2 = 102.7$ GPa, $\beta_3 = -818$ GPa, and $\beta_4 = 887.8$ GPa. In literature the reported values of Young's modulus obtained from computational studies range from 53 to 220 GPa [30–33,39] and the experimental values range from 69 to 73 GPa [34–37]. From our MD data, the maximum stress or the ideal strength is found to be 11.42 GPa. The reported values of strength obtained from computational studies range from 10.8 to 65 GPa [30–33], and the available experimental values range from 3.4 to 12.9 GPa [34,36,38,67]. It is evident that our results on the Young's modulus and ideal strength agree reasonably well with the available experimental data.

To determine size dependence of the stress-strain response of aSiO$_2$, we considered four different domain sizes and compared their strength and toughness. As shown in Fig. 2, we find that both strength and toughness are well converged for domains larger than 300 000 atoms. For smaller domain size, the nanocracks nucleating in the domain interact with its periodic images, which reduces its strength and toughness. As size increases, the nucleating sites act as isolated sites and the behavior of the domain becomes insensitive to the domain size. The size-dependent mechanical behavior can thus be attributed to the elastic interactions that take place across the domain's periodic directions.

B. Crack nucleation in amorphous silica

To understand the crack-nucleation process, we investigate the atomistic fields of the potential energy, the components of the virial stress tensor for each atom in the domain as well as their kinetic energy—both of which are directly obtainable from MD simulations. The virial stress tensor components and potential energy fields do not clearly indicate any nucleation event, until a nanocrack of around 1 nm length is

formed. Due to the presence of highly heterogeneous stress states and amorphous atomistic structure, it is difficult to identify any signatures of the nucleation process from the atomistic information on energy or force. However, a clear thermal blueprint appears at the onset of the crack nucleation process, as illustrated in Fig. 3. A diagonal thermal pattern evolves at the onset of crack nucleation—and the temperature surrounding the nucleating site is much higher than that in the remainder of the domain.

The gradient in thermal state surrounding the nucleation site evolves from the bond rupture process that releases elastic energy in the form of heat and creates new surfaces consisting of atoms with dangling bonds and higher potential energy. Although the thermal pattern developed during the deformation process does not show any strong correlation with the composition or deformation field, the wider spatial distribution of the thermal patch shows the possibility of a spatially distributed breeding ground for the formation of one or a series of nanocracks (if the domain is bigger). As soon as one nanocrack emerges in the thermally active regime, a rapid bond-breaking event emerges surrounding the
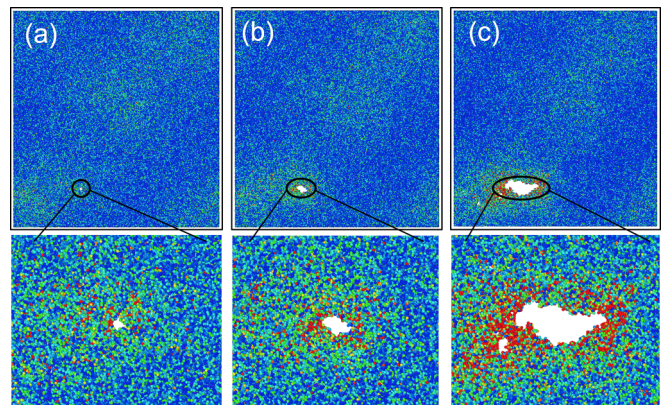
FIG. 3. Thermal map during the localized nucleation of nanocrack at random location in the domain. The images represent the temperature fields at (a) $\epsilon_{yy} = 0.325$, (b) 0.335, and (c) 0.340. The temperature range in the domain is 298–305 K, with the maximum appearing along the material edge at the crack-nucleation site.
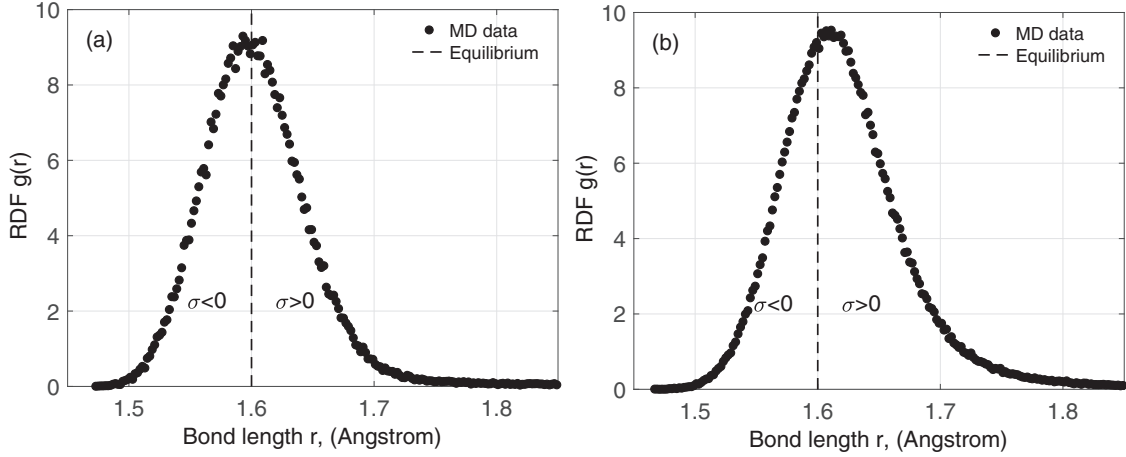
FIG. 4. Tension-compression asymmetry in the radial distribution function $g(r)$ in Si-O bond distribution around the average nearest-neighbor bond distance of 1.60 Å: (a) at the undeformed amorphous state and (b) at the 30% strain state. The tensile and compressive regions are indicated by $\sigma > 0$ and $\sigma < 0$, respectively. The vertical dashed line indicates the median Si-O bond length of 1.60 Å of the undeformed state.

nanocrack. Initiation of nanocracks reduces the elastic energy at the nucleating site followed by an elastic relaxation that extends rapidly into the neighboring regime, triggering a catastrophic material separation process (as evident in the stress-strain response of the domain in Fig. 1).

To investigate the bond deformation process (involving stretching or contraction in length), we calculate the radial distribution function (RDF) at two strain states. As illustrated in Fig. 4, at 30% strain (close to the crack nucleation strain state), the distribution in RDF becomes notably asymmetric, indicating a higher number of bonds in the tensile state than in the compressive state. The minimum and maximum bond lengths at this deformed state are around 1.50 and 1.81 Å, respectively; whereas at the undeformed state, $\epsilon_{yy} = 0$, the distribution is near-symmetric around the equilibrium bond length indicating the equivalence of the tensile and compressive stress states of the Si-O bonds. The minimum and maximum bond lengths are around 1.47 and 1.74 Å, respectively, which are around 7.5% on either side of the equilibrium Si-O bond length. The average bond length is 1.599 Å at $\epsilon_{yy} = 0$ and 1.613 Å at $\epsilon_{yy} = 30\%$ indicating a net increase in the average bond length with increased deformation. The net alteration of the bond lengths is tensile as such the domain exhibits a small volumetric expansion. At the onset of nanocrack nucleation, the bond length distribution reaches the widest distribution, with only a fraction of the bonds reaching the maximum bond length at the nucleation site. As the domain relaxes the elastic energy surrounding the nucleation site, the bond lengths start approaching the equilibrium value at the site. Moreover, during the nucleation process the tetrahedral units retain their tetrahedral structures but undergo reorientation at their connecting sites. To elucidate the role of the individual atoms on the deformation process and explain the nucleation events, we explore the mechanical state of the atoms in terms of atomistic variables and develop a species-dependent picture of the underlying mechanisms in the following section.

1. Atomistic mechanisms governing crack nucleation

a. Determining stress state at the atomic scale. From the MD simulations information is available on both the temporal and spatial evolution of the classical phase space constructed by the position and momenta of all the particles. The microscopic formula used to describe the pressure or average stress of a classical (or quantum) system of interacting particles is known as the virial stress, which is defined mathematically as the following:

$$\sigma_{\text{virial}} = \frac{1}{V}\left(-\sum_i m_i \vec{v}_i \otimes \vec{v}_i + \sum_{i \neq j}(1/\beta)\vec{r}_{ij} \otimes \vec{F}_{ij}\right), \quad (2)$$

where m_i and v_i are the atomic masses and velocities, respectively, r_{ij} and F_{ij} are distance and force between the atoms at i and j, respectively; $\beta = 2, 3, 4$ for pairwise, three-body, and dihedral interactions, respectively [68,69]; and V is the volume of the entire domain. Equation (2) provides an average measure of stress for the entire domain. It accounts for the velocities and interaction forces of all the atoms in the sum. The first part of the expression involves the kinetic energy of the individual atoms and the second the "virial" or interaction force of each atom with its neighbors. We denote them as $\sigma_{\text{virial}}^{\text{k}}$ and $\sigma_{\text{virial}}^{\text{p}}$, respectively.

The virial stress formula has a strong statistical mechanical foundation and served inarguably as one of the key formulas in describing the mechanical behavior of a collection of interacting particles [70–78]. Nonetheless, its application in describing a continuum measure of stress, $\sigma(\mathbf{r})$, (also known as the Cauchy stress) at an arbitrary material point of the atomistic domain has been a subject of active research and debate [69,74–76,79,80]. Determination of the Cauchy stress involves averaging of the properties of the particles at the neighborhood of observation point $\mathbf{r}$ at time t [72,73,80]. There exists some arbitrariness in selecting the neighborhood in extracting a continuum scale description of stress from the atomic quantities [76,80]. Irving and Kirkwood [71]

suggested to consider "a spatial average over a microscopically large though macroscopically small domain" and Hardy [73] offered a practical guide for many-body potentials "the range of inter-particle interactions should be less than the range of the spatial averaging." While averaging of atomic properties at a material point has been shown to be powerful in obtaining a thermodynamically and mechanically consistent continuum description of local stress, it comes at the cost of smoothening out local characteristic features that may play a crucial role in situations (such as around dislocation cores or a propagating or evolving crack tip) wherein sharp stress gradients at the atomic scale governs the macroscopic behavior of the system, particularly under deformed condition. This has been elaborated in greater details recently for a number of defective atomistic systems [74,81].

Since the material system under consideration in this article is amorphous and the focus of our study is to extract atomic scale processes that regulate crack nucleation and propagation, we employ both the virial and Hardy descriptions of atomic and continuum stress respectively. The former is used to construct a detailed atomistic picture of the nucleation process in terms of the kinetic and potential energy parts of virial stress, and the latter is used to develop a continuum scale understanding of the crack propagation process. The virial stress is calculated from the virial stress components of each atom: $\sigma^{\text{virial}} = \sum_i^N \sigma_i^{\text{virial}}/(Nv)$, σ_i^{virial} is the virial stress at atom i, N is the total number of atoms in the domain, and v is the effective atomic volume per atom (such that $V = Nv$). We obtain σ_i^{virial} directly from LAMMPS simulation. The effective atomic volume v is computed by satisfying the condition that the MD-given macroscopic stress σ^{macro} is equal to σ^{virial}. To determine a Hardy estimate of the Cauchy stress (that represents an average measure of the atomic stress at each atomic site), a set of neighbors within a cutoff distance R_c is considered, which gives the mathematical expression for the Hardy stress at atomic site i as the following:

$$\sigma_i^{\text{Hardy}} = \sum_{i=1}^{M} \frac{\sigma_i^{\text{virial}}}{M}, \tag{3}$$

where M is the number of atoms within the cutoff distance R_c. The average macroscopic Hardy stress computed over the entire domain is thus $\sigma^{\text{Hardy}} = \sum_i \sigma_i^{\text{Hardy}}/(Nv)$. Following Hardy's recommendation [73], an approximation for the cutoff distance R_c can be made by calculating the interatomic distance beyond which the interaction energy is zero. With the ReaxFF potential for silica this distance is 3.2 Å, as shown in Fig. 5.

To assess the accuracy of R_c in reproducing the continuum scale behavior of the domain, we perform the coordination analysis for all the bonds in the domain as well as for the O-O and Si-Si bonds separately, up to a distance of 9 Å. As shown in Fig. 6, the atomic correlation approaches a constant value at $r > 5.0$ Å, indicating insensitivity of the atomic scale features beyond this length. It is thus reasonable to conclude that for a distance of $R_c = 5.0$ Å, the Hardy approximation of Cauchy stress at the atomic sites provides a converged estimation. (We show later that this value of R_c holds even for the domain under crack propagation.)
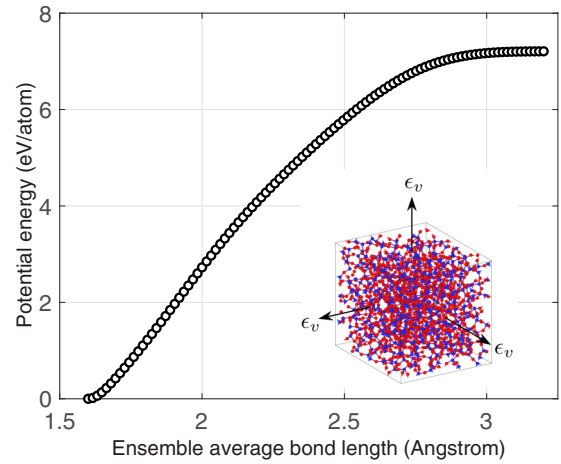
FIG. 5. Interaction potential energy of the amorphous domain containing as a function of the average bond length obtained by applying hydrostatic deformation to the domain. The loading condition is shown in the inset.

To determine the applicability of virial stress and Hardy stress in obtaining macroscopic stress-strain behavior of the domain, in Fig. 7, the uniaxial stress-strain relation of silica obtained from the system pressure p_{yy}, the virial stresses of the atoms σ_i^{virial} and the Hardy stresses at the atomic sites σ_i^{hardy} are compared. It is seen that for an "effective atomic volume" of 13.1 Å^3 both the virial and Hardy stresses provide consistent macroscopic stress of the domain suggesting the equivalence of the following relationship: $\sigma^{\text{macro}} = \sigma^{\text{virial}} = \sigma^{\text{Hardy}}$, where the ingredients of σ^{virial} are virial stresses at the atoms and the ingredients of σ^{hardy} are the spatial average of the virial stresses at each of the atomic sites integrated over a spherical volume of $4\pi R_c^3/3$. Our results therefore suggest that for amorphous silica $\sum_i^N \sigma_i^{\text{virial}} = \sum_i^N \sigma_i^{\text{Hardy}}$, although $\sigma_i^{\text{virial}} \neq \sigma_i^{\text{Hardy}}$. It is noteworthy that, in spite of the differences in virial and hardy stresses at the atoms or atomic sites, their ensemble spatial and temporal averages give an identical measure of macroscopic stress state of the domain. Thus either of the virial stress or Hardy stress estimates can be used to obtain the macroscopic stress-strain behavior of the domain. Nonetheless local atomic scale features are better reflected in the virial structure, as it directly correlates with the momentum of the particles and their interactions with neighbors. Spatial averaging can wash out species-dependent attributes of atomic interactions as we shown in the next section.

b. Species-dependent stress state. One of our primary objectives is to explore the role of Si and O atoms on the physics of mechanical deformation in amorphous silica. The number of O atoms is twice the number of Si atoms in the domain. Each tetrahedron is composed of one Si atom and four O atoms, and each O atom connects two tetrahedrons. While Si atoms are the nearest neighbors of O atoms and vice versa, their second nearest neighbors differ in terms of number and species type. The Si atoms have O as their second nearest neighbors, whereas the O atoms have O as the second nearest neighbors, as evident from the RDF plots shown in
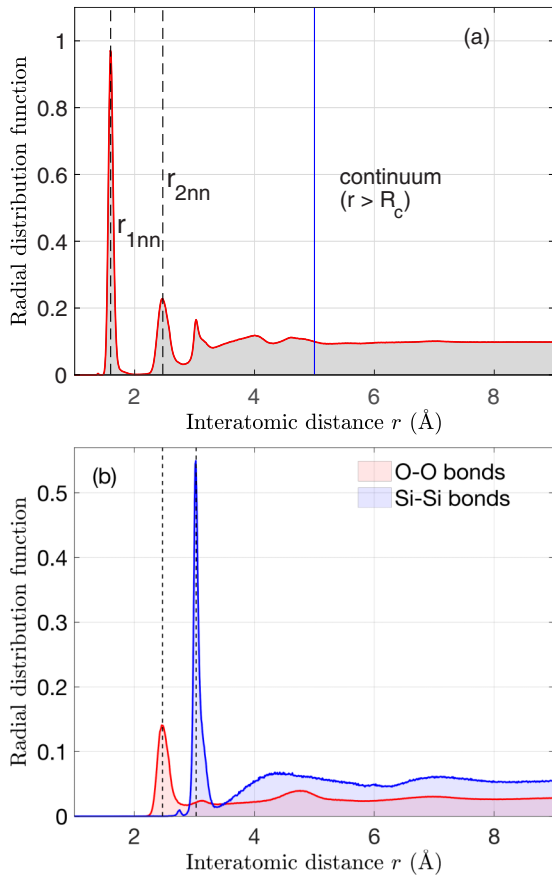
FIG. 6. (a) Radial distribution function in a domain containing around 1 million atoms. The vertical dashed lines indicate the interatomic distances at the first-nearest-neighbor and the second-nearest-neighbor distances, denoted by r_{1nn} and r_{2nn}, respectively. The blue solid line denotes the value of the interatomic distance above which the atomic structure behaves like a continuum media. (b) RDF for the individual species (Si and O) in the domain.

Fig. 6. Thus the second-neighbor interactions at the Si and O atoms are markedly different. While the Si-O interactions produce identical force along the Si-O bonds, the dissimilar
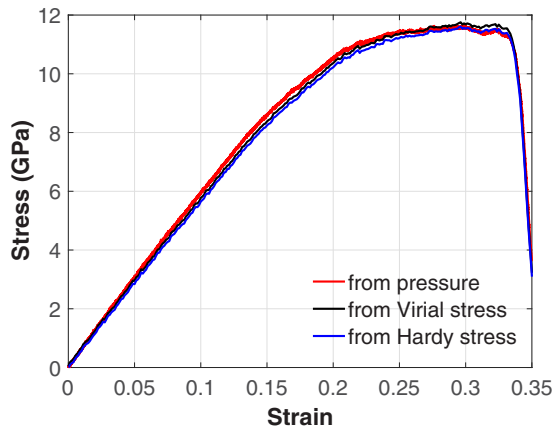
FIG. 7. Stress-strain response of amorphous silica obtained from system pressure, virial atomic stress, and Hardy stress at the atomic sites.

second- and third-nearest-neighbor interactions have the potential to produce distinct interaction forces for the O and Si atoms. It is thus important to determine how the O and Si atoms carry or share load at different stages of the deformation process so that the macroscopic failure of silica can be altered by invoking species-dependent treatments at the atomic scale. To determine the role of the individual species on the overall deformation behavior of the silica matrix, we explore the virial and hardy descriptions of stresses at the atoms and atomic sites, respectively. (To distinguish them, we used "virial stress at atoms" and "Hardy stress at an atomic site," following the methodology applied to determine them.)

To assess the tensile versus compressive stress state at a macroscopic strain state of ϵ_{yy}, the atoms are classified into four groups:

$$N_i^{\text{tension}}(\epsilon_{yy}) = \int_0^\infty n_i(\sigma > 0, \epsilon_{yy}) d\sigma, \tag{4}$$

$$N_i^{\text{compression}}(\epsilon_{yy}) = \int_0^\infty n_i(\sigma < 0, \epsilon_{yy}) d\sigma, \tag{5}$$

$$N_{\text{SiO}_2} = \sum_{i=1}^2 \int_0^\infty n_i(\sigma) d\sigma, \tag{6}$$

where i is the species index—it is either Si or O; and σ_i is the virial/Hardy atomic stress, and N_{SiO_2} is the total number of atoms in the domain. As shown in Fig. 8, both virial stress and Hardy stress estimates show the stress states to be highly heterogeneous (under deformed and undeformed configurations), indicating a larger fraction of the Si and O atoms to carry moderate stresses and smaller fraction to carry higher/lower stresses. Nevertheless distinct stress states for the virial and Hardy estimates are notable in terms of the proportions of the atoms or atomic sites representing the tensile versus compressive states.

At the undeformed state, the atomic stresses are nonzero in the domain, although the macroscopic stress in the domain is zero (as can be seen in Fig. 7). This is due to the thermodynamic processing that the domain underwent in the amorphization process which breaks the crystallinity of the solid and makes some bonds elongated and some contracted (as evident from Fig. 4). As expected, the Hardy estimate eliminates the local stress structure of the atoms through averaging over a spherical volume of $4\pi R_c^3/3$, within which both Si and O atoms are present. Since it produces an average stress-measure over multiple species (which in this case are O and Si), it makes it difficult to interpret the average measure in terms of the individual species and their species-dependent atomic structure. For monocomponent and crystalline materials, the averaging may not die out any atomic properties, but for materials like silica (which has a notable difference in terms of its specifies-dependent atomistic structure and long-range interactions) it is important to retain the heterogeneous atomic attributes fully to understand atomic interactions and their macroscopic consequence. In complex heterogeneous media, the virial scheme can thus offer a robust pathway for uncovering the role of individual species and their interaction details on macroscopic deformation. However, the Hardly estimates can serve as a powerful tool for developing a continuum scale understanding deformation behavior, as we
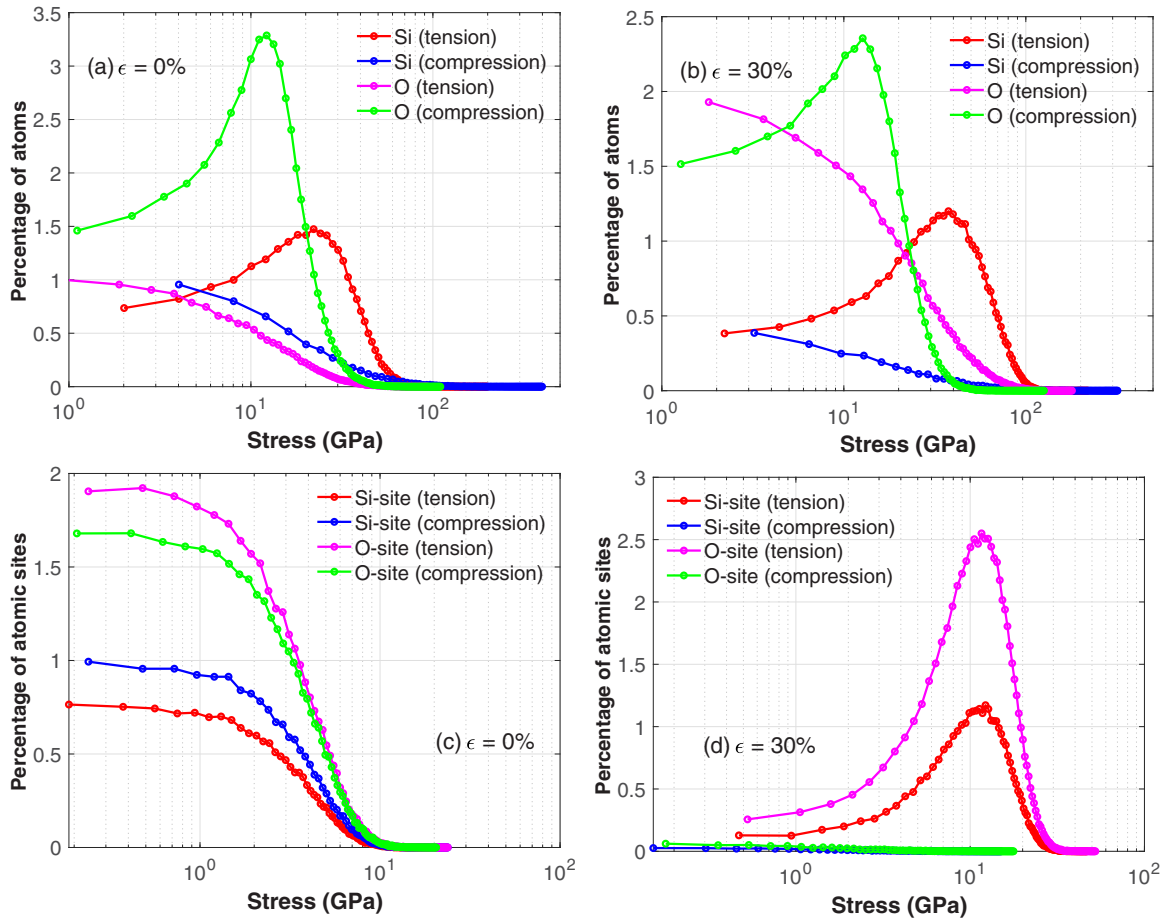
FIG. 8. [(a) and (b)] virial stress estimates at the Si and O atoms under tension and compression, shown in terms of the percentage of the total atoms, at $\epsilon_{yy} = 0$ and $\epsilon_{yy} = 30\%$ macroscopic strain. [(c) and (d)] Hardy stress-estimates at the Si and O atomic sites decomposed into tensile and compressive stress states at $\epsilon_{yy} = 0$ and $\epsilon_{yy} = 30\%$ macroscopic strain.

demonstrated later in Sec. III C in the context of calculating fracture toughness.

Based on virial stress structure of atomic interactions, the Si atoms are the majority tensile stress carriers and the O atoms are the majority compressive stress carriers at both of the strain extrema: $\epsilon_{yy} = 0$ and 30%. While some fraction of Si atoms are in tension and some in compression, the number of Si atoms in tension is substantially higher than that in compression. Conversely the number of O atoms in compression is substantially higher than that in tension. At a given loading state, the highest percentage of Si or O atoms stay at an intermediate stress level, a few percentage carry the highest stress, and the remaining atoms carry a range of lower stress. For the O atoms, the stress levels of the atoms in the intermediate-to-higher stress range go up with increased loading, while the atoms at lower stress levels are less affected by applied deformation. On the other hand, for the Si atoms, most of them substantial alteration of their stress state. In can be argued if atoms under stress has any meaning, considering bonds are usually referred to having extension or contraction representing the state of tension and compression. As each atom has multiple bonds (first, second, third nearest neighbors, etc.) form with different neighbors within the interaction distance and the bond lengths are distributed over a range, it is a nontrivial task to compute stretching and contraction of each

bond and describe the deformation process in terms of those. The virial stress components of the atoms can be interpreted as an effective measure of tensile and compressive stress states of all the bonds of an atom. Thus in the remainder of the article we use the term "stressed atom" to denote the resultant effect of bond contraction and stretching for the atom.

c. Understanding nucleation from virial stress structure (VSS). Analyzing the stress fields, one of the striking features that we observe at the higher deformation states and during the nucleation process is the appearance of nanoscale fibrous patterns in the virial stress fields, as illustrated in Fig. 9. NF9We call them *stress-fibers*, as stress serves as the underlying basis. These stress-fibers are comprised of atoms with highest stress states in the domain. It is evident that they are finite in length (of less than a few nanometers). Also, they are aligned along the loading direction and made of alternating assembly of Si and O atoms. The atoms in between the stress-fibers are at a lower energetic states than those in the fibers. Their intensity is the highest at the growing nucleated crack front. The atoms in the upper and lower sides of the nanocrack, marked by "stress relaxation regime," relaxes the elastic energy substantially and do not form stress-fibers. The evolving nanocrack interacts with the fibrous stress field continuously throughout the material separation process.
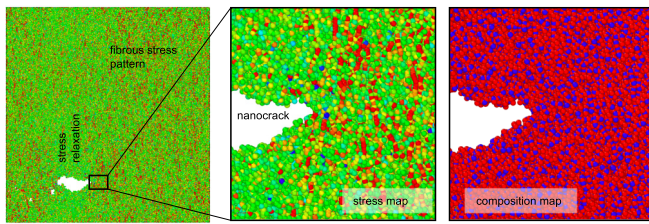
FIG. 9. The stress field of the normal atomic stress σ_{yy} at a macroscopic strain state of 30%. Middle plot shows zoomed in view of fibrous stress patterns around the incipient nanocrack. The corresponding composition map is shown on the right.

With an aim of identifying a distinctive atomistic feature that connects directly to the condition of crack nucleation and propagation in amorphous silica we explored the atomistic fields of potential energy, kinetic energy, virial stress fields, components of the forces, and hardy stress fields. We found a well-identifiable feature only from the virial stress. While the kinetic energy was indicative of the region where the crack starts to form, the virial structure indicated species-dependent atomic features that connect to the nucleation process. The Hardy stress field however did not show any evidence of species-dependent atomistic attributes that could be used to describe definitively the nucleation process.

To build a quantitative and structural understanding of the virial stress-fibers, we compute the average length of these fibers in the domain as a function of its macroscopic strain state. As illustrated in Fig. 10, the length of the virial stress-fibers increases with strain followed by a saturation in length of around 2.0 nm around the maximum macroscopic stress state of the domain. The density of the stress-fibers however continues to increase until the nucleation process kicks in. The density is calculated by counting the number of fibers in the domain and dividing it by the volume of the domain. It is noted that at around 0.9 fibers per nm^{-3} the domain undergoes a rapid atomistic bond process, leading to fracture.

The stress-fibers are the majority of the load carriers and their finite lengths allow accommodation of deformational energy through rotation of the adjoining tetrahedral units. Since the domain preserves the structure of the tetrahedral units, alteration of Si and O bonds that configure the backbone of the tetrahedral units enables reorientation of the units at the connecting sites when loaded along the longitudinal axis of the fibers. This highlights an important point that the silica tetrahedra are highly stable and maintain their coordination number. They play a significant role in absorbing and distributing the elastic energy and transfer load through a complex intermingled network of tetrahedra assembled in spatially distributed interacting stress-fibers. Furthermore, computing $N_i^{tension}(\epsilon_{yy})$ and $N_i^{compression}(\epsilon_{yy})$, with i denoting Si or O, at 15 different macroscopic strain states with a regular interval between $\epsilon_{yy} = 0$ to 0.3, we find that there's a smooth and continuous trend in load sharing by the stress carriers, as shown in Fig. 11. Throughout the entire deformation history, Si atoms are the majority tensile load carriers, whereas the O atoms act as the majority compressive load carriers. Also, the difference in the number of O atoms carrying the tensile and compressive stresses reduces dramatically at higher loading,
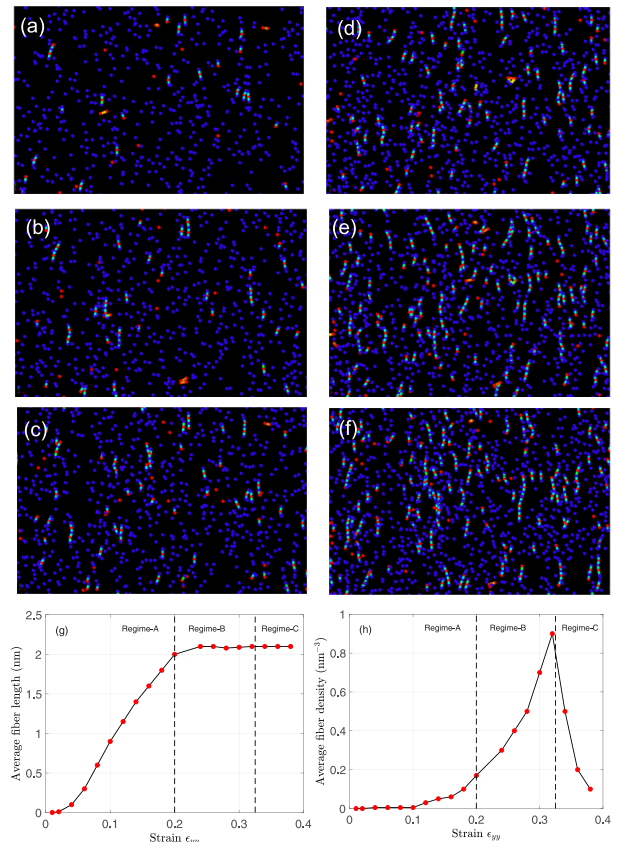
FIG. 10. Stages of virial stress-fiber formation at different strain states of the domain. (a) $\epsilon_{yy} = 7.5\%$, (b) 10%, (c) 12.5%, (d) 15%, (e) 17.5%, and (f) 20%. Blue atoms represent O and red atoms Si. Atoms with stresses higher than a are shown to highlight the highly stressed atoms. (g) Average stress-fiber length as a function of applied strain ϵ_{yy}. (h) Average fiber density as a function of applied strain ϵ_{yy}. Regimes A, B, and C correspond to the strain windows of $0.0 \leqslant \epsilon \leqslant 0.21$, $0.21 \leqslant \epsilon \leqslant 0.32$, and $0.32 \leqslant \epsilon$, respectively.

whereas for the Si atoms, the difference keeps growing, as evident from as shown in Fig. 11(b).

Heterogeneity in atomic stress is thus higher for O at the undeformed state and it reduces substantially with increased loading. On the other hand, for Si heterogeneity in its atomic stress grows with increased loading. The tensile and compressive stress states of the Si atoms becomes less sensitive to deformation beyond $\epsilon_{yy} = 15\%$, while the number of O-atoms carrying tensile (compressive) load continues to change up to $\epsilon_{yy} = 21\%$. Nonetheless, for deformation larger than $\epsilon_{yy} > 0.21$, the number of tensile and compressive stress carrier Si and O atoms reach a saturated value. This feature is directly connected with the corresponding macroscopic stress states (shown in Fig. 1). The energy coming from continued loading at the remote boundary during $21\% \leqslant \epsilon_{yy} \leqslant 32.5\%$ is absorbed by the reorientation or reorganization of the tetrahedral units in the stress-fibers. Formation of stress-fibers takes place during $15\% \leqslant \epsilon_{yy} \leqslant 21\%$, and rotation of the tetrahedra takes place during $21\% \leqslant \epsilon_{yy} \leqslant 32.5\%$.

Although the description of virial stress as a continuum measure of stress has been a matter of active debate, our results and analysis show that it is possible to exploit the virial
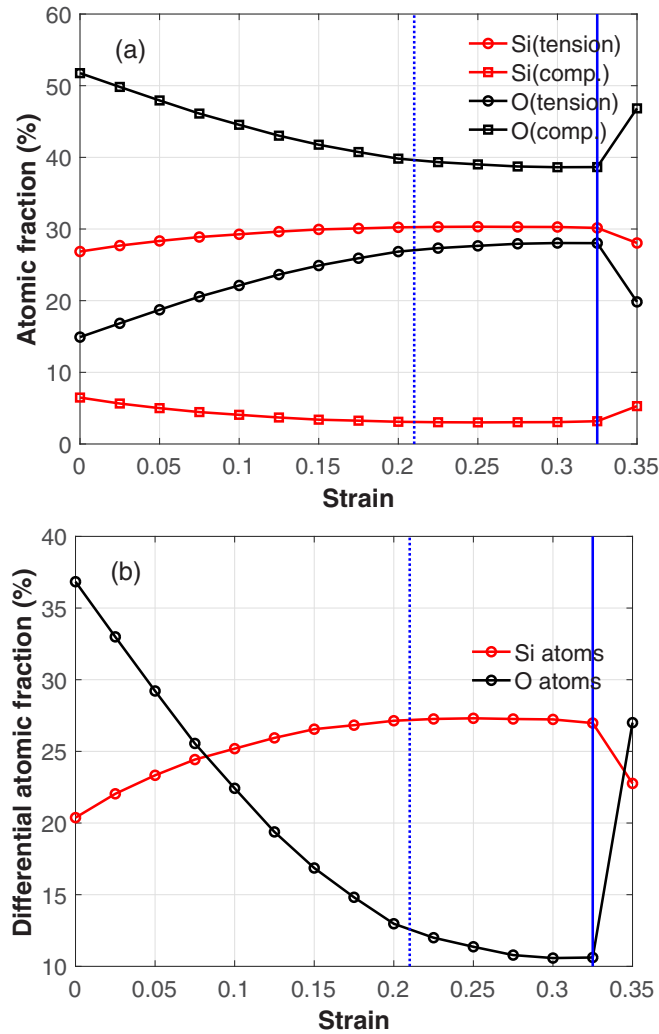
FIG. 11. (a) Fraction of the atoms, $N_i^{\text{tension}}(\epsilon_{yy})$ and $N_i^{\text{compression}}(\epsilon_{yy})$, taking tensile and compressive stress at different loading states, respectively; where i is Si or O. (b) Differential atomic fraction, $\Delta N_i(\epsilon_{yy}) = |(N_i^{\text{tension}}(\epsilon_{yy}) - N_i^{\text{compression}}(\epsilon_{yy})|$, representing the difference in number of atoms in tensile and compressive stress states. The vertical dashed line at $\epsilon_{yy} = 0.21$ indicates the activation of the irreversible deformation process, and the solid line at $\epsilon_{yy} = 0.325$ indicates onset of crack nucleation.

stress structure as an atomistic ingredient for characterizing the condition for bond rupture process leading to fracture. Unlike homogeneous materials (wherein virial stress is uniform among the specie), in amorphous silica virial stress is distributed in a discontinuous manner, particularly at higher deformation. Interestingly these virial stress-fibers have a direct connection to the condition of crack nucleation and propagation. The fibrous pattern in virial stress fields reveals how the interatomic forces at the Si and O atoms evolve over the deformation process.

To check the possible effects of cooling rate and melting temperature, we investigated both of these effects for a number of cooling rates: 0.24, 0.12, 0.024, and 0.012 K/fs and melting temperatures: 3000, 5000, 8000, and 12 000 K. In all cases, heterogeneity or inhomogeneity in atomic stress is

present in the domain that induces distributed locations of high-stress pockets at random locations in the media. The highly heterogeneous stress distribution configures the stress-fibers. Moreover, investigation of the atomic stress distribution indicates that the cooling rate and melting temperature have negligible effect on both the compressive and tensile stress states of the O atoms; whereas for the Si atoms, their compressive stress states are unaffected but their tensile stress states are affected by the melting temperature. From these observations, we conclude that crack nucleation manifests as a rich atomistic process that involves formation of highly heterogeneous stress-fibers, followed by reorientation of the tetrahedral units aligned along the stress-fibers. Next we explore these mechanisms in the context of crack propagation.

C. Crack propagation in amorphous silica

In this section, we focus on determining the role of individual species on propagation of an initial crack in a domain, with or without the presence of a nanopore. Although the macroscopic stress-strain behavior of pristine silica has been reported widely in the literature (as discussed in the introduction section), analogous studies on crack propagation remain inadequate [82–85]. To unveil the atomistic mechanisms governing crack propagation criteria, we consider an initial crack of finite length a_0 in the domain and included small-diameter porosities to predict its role on crack propagation.

1. Crack propagation in pristine aSiO₂

The condition for crack propagation is investigated by (a) placing a straight crack of length a_0 at the left edge of the amorphous domain, (b) applying a monotonically increasing uniform load σ_∞ at the remote boundary, and (c) identifying the maximum stress at which the crack starts propagating in the domain. Before conducting simulations with an initial crack, we perform uniaxial stress test in the domain containing the edges only, to assess the relative influence of edge and crack on effective mechanical properties of amorphous silica. The configurations along with their stress-strain curves are shown in Fig. 12. For either configurations, the simulation domain is taken periodic along the loading direction and the out-of-plane direction and an empty space is added along the third direction to avoid interactions between the periodic images of the domain.

From the macroscopic data, the maximum stress point is located to appear at $\epsilon_{yy} = 0.12$. The effective stiffness of the domain "with the edges only" (but no crack) is 68.952 GPa. For the "domain with the edges and a crack" of length 100 nm stiffness is 65.581 GPa. The strengths of the domains for the corresponding configurations are 11.22 and 6.902 GPa, respectively. Compared to bulk amorphous silica (which has stiffness and strength of 69.0 and 11.42 GPa, respectively), the domain "with edges but no initial crack" shows very similar elastic behavior in the linear regime of mechanical deformation—but the presence of an initial crack reduces the stiffness of the domain by around 5% only and the strength by 39%. The highest elastic energy density or the integrated area under the stress-strain curve, denoted here as $\Pi_c = \int_0^{\epsilon_{\text{fracture}}} \sigma(\epsilon_{yy}) d\sigma$ is found to be 0.632 J m^{-3} for the "domain with the crack," 1.606 J m^{-3} for the "domain with the edge but
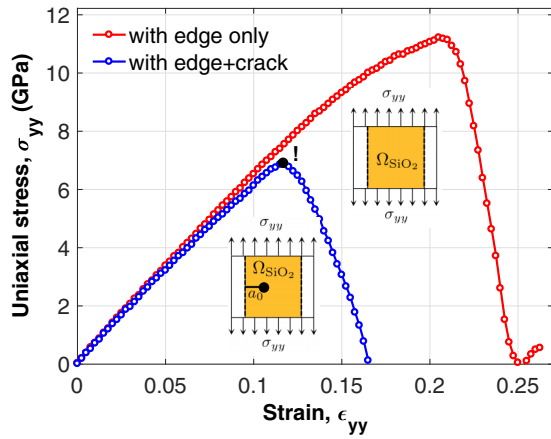
FIG. 12. Comparison of the stress-strain curves obtained from the uniaxial tensile test of an amorphous silica domain ($962.1 \times 832.8 \times 16.3$ Å^3, which contains 1 080 000 atoms) "with two edges" and "with two edges and a crack" of length 100 Å, as defined in schematics in the inset. The maximum stress state appearing at $\epsilon = 12\%$ is identified by "X'.

no crack," and 3.143 J m^{-3} for the "domain without any crack or edge." These numbers suggest that the presence of edge makes no significant effect on strength—but it has a sizable effect on Π_c. An edge reduces Π_c of pristine amorphous silica by 50% and an initial crack of length 100 nm reduces it by around 80%. To explore the atomistic events that lead to fracture of the domain, we investigate the atomic scale processes in the domain and its evolution near the maximum stress point "X" (identified in Fig. 12). To capture the first bond rupture event, we calculate the Lagrangian displacement of all atoms over the entire deformation history and determine the maximum change in the first-nearest-neighbor distance for each species (Si and O), as illustrated in Fig. 13.
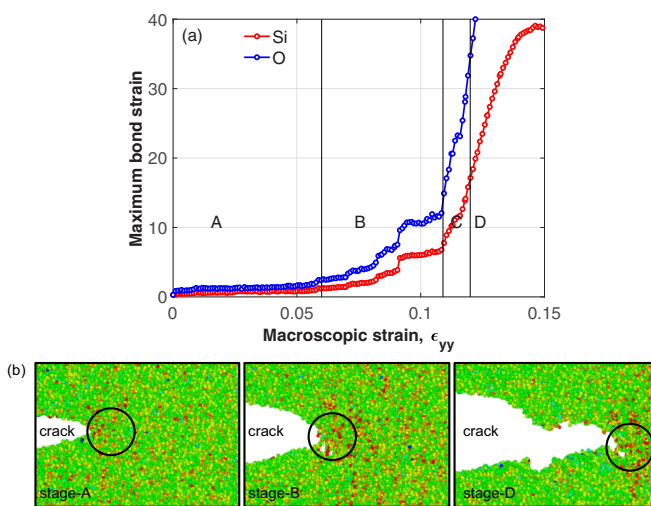
FIG. 13. (a) Evolution of maximum bond strain at different stages of the macroscopic loading for $0.0 \leqslant \epsilon_{yy} \leqslant 0.15$. Four distinct fracture stages are identified by stages A, B, C, and D. (b) The corresponding atomic configurations of stages A, B, and D along with the atomic stress field σ_{yy} in the bottom panel. The circles identify the process zone at the crack tip.

The results show that a small number of the nearest-neighbor bonds for both Si and O at the neighborhood of the crack tip are subject to rupture at a much earlier stage in the deformation history than what is apparent from the macroscopic stress-strain data. Yet such localized bond rupture does not immediate lead to a propagation of the initial crack. Based on how far the atoms configuring the first bond rupture event go, we identify four distinct failure stages at the atomic scale: they are marked by A, B, C, and D. In stage A, denoted by $0.0 \leqslant \epsilon_{yy} \leqslant 0.07$, bonds are stretched uniformly in the domain; in stage B, denoted by $0.07 \leqslant \epsilon_{yy} \leqslant 0.109$, a few bonds fracture locally and subject to reconstruction in front of the crack tip; in stage C, denoted by $0.109 \leqslant \epsilon_{yy} \leqslant 0.12$, a number of bonds undergo rapid failure. The macroscopic stress-strain data (Fig. 12) show the onset of the fracture event at around $\epsilon_{yy} = 0.12$, whereas the bonds at the crack tip starts breaking at a rapid rate in regime C at $\epsilon_{yy} = 0.109$, which is much earlier than what is visible in the macroscopic stress-strain curve. Also, a small number of bonds rupture locally in stage B—yet it is only stage D, denoted by $\epsilon_{yy} \geqslant 0.12$, wherein fracture of the domain becomes noticeable in the macroscopic stress-strain behavior.

Although in stage B a limited number of bonds (2 to 3 around the crack tip) locally fracture much earlier, at $\epsilon_{yy} = 0.06$, they do not release sufficient elastic energy for continued breaking of the bonds ahead of the crack tip. Newly formed stress-fibers offer resistance to the continued propagation, so we attribute the appearance of stage B as a direct consequence of the formation of stress-fibers and their increased intensity surrounding the crack tip. Analyzing the atomic stress fields and composition maps, we find that the stress-fibers of lengths around 1 nm are formed by an assembly of Si and O atoms at higher deformation during stage B, as shown in Fig. 14.

Due to the fibrous stress patterns, the matrix in front of the crack tip ruptures sequentially—and when sufficient number of links between the tetrahedral units are broken, the elastic energy at the crack tip becomes large enough to lead a rapid growth of the initial crack. The rapid growth process takes place in stage C, and in stage B, the virial stress-fibers continue to form and break, mediated by a spontaneous reconstruction process at the crack tip. This unveils an important point that the onset of crack nucleation is a localized event and undetectable from the macroscopic data. Unlike crystalline brittle solids (which undergo rapid growth of the bond rupturing process), silica takes some time between the onset of nanocrack nucleation and the time at which the macroscopic failure becomes detectable.

To determine the role of O and Si atoms in the deformation process, we explore the distribution of their stresses at two different loading states that cover the elastically deformed state (stage A) and the transition state (stage B), as shown in Fig. 15. It is found that the virial stress fields exhibit heterogeneity in atomic interaction, whereas the Hardy stress distribution averages out the species-dependent stress distribution features of the domain. The difference in percentage of atomic sites at the Si and O atomic sites can be attributed to the number of Si and O atoms. While it preserves the heterogeneous character of the stress-fields at the continuum scale, the local atomic characters are lost in the process.
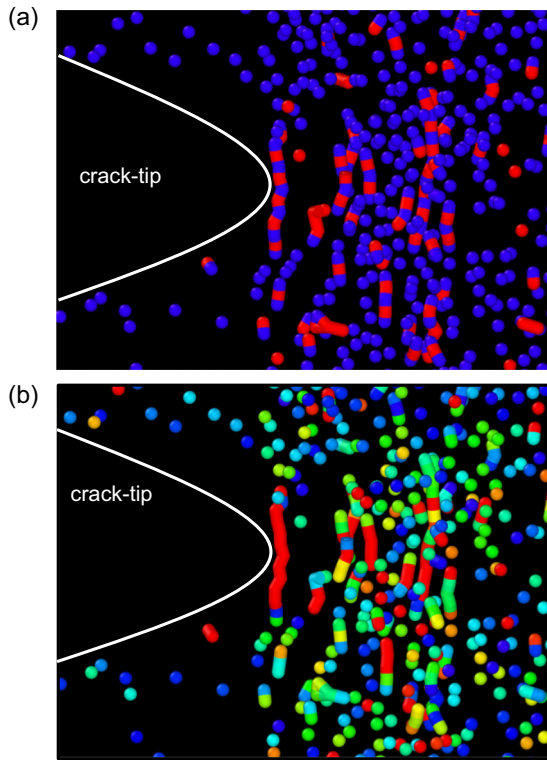
FIG. 14. (a) Composition map of atoms with higher virial stress at the crack tip, showing formation of nanoscale chains comprising alternate assembly of Si atoms (shown in blue) and O atoms (shown in red). (b) Normal stress states at the crack tip. Only the atoms with virial stresses higher than 50 GPa (shown in blue) is used to construct the image to reveal primary tensile stress carrier atoms. The highest stress in the stress-fiber is around 60 GPa (shown in red).

a. Fracture toughness. To estimate a measure of fracture toughness we use two approaches. First we use the Irwin's formula that relates the critical stress-intensity factor with fracture strength: $K_{IC} = \sigma_{max}\sqrt{\pi a_0} f(a_0/w)$ [86], where σ_{max} is the maximum macroscopic stress, a_0 is the initial crack length, and w is the width of the domain normal to the loading direction. From our MD simulations (as exhibited in Fig. 12), we find the maximum stress to be equal to 6.9 GPa, the effective stiffness of the domain is 65.5 GPa, the ratio between half of the height and width at the highest stress state is around 0.51, and the ratio between the crack-length and the width is 0.11. These values give $K_{IC} = \sigma_{max} \times \sqrt{\pi a_0} f(a_0/w) = \sigma_{max} \times \sqrt{\pi a_0}(1.122 - 0.231 a_0/w) = 1.22 \times 1.09 = 1.32$ MPa$\sqrt{m}$. The available experimental values of K_{IC} of silica include 0.77 ± 0.16 MPa$\sqrt{m}$ [87] in thin-film silica (with a fracture strength of 0.81 GPa) and 1.0 MPa $\sqrt{m}$ for silica fiber (with a fracture strength of 3.5 GPa) [36]. The disagreement among the values of K_{IC} may originate from the discrepancy in values of fracture strength and approximations in the empirical factor $f(a_0/w)$. Furthermore, from the classical theory of linearly elastic fracture mechanics, the relation $K_{IC} = \sigma_{max}\sqrt{\pi a_0} f(a_0/w)$ is built on the crack tip stress profile that varies as $1/\sqrt{r}$ from the crack tip [88], and the fracture strength varies as $1/\sqrt{a_0}$ with respect to the crack length a_0. Next we investigate these two relations in details.

Figure 16 shows a continuum representation of the normal stress field $\sigma_{yy}(x, y)$ over the entire domain at the onset of crack propagation. The stress field is obtained by averaging the stresses of the atoms in the xy plane over a uniformly discretized a 5-Å mesh. We separately use the virial and Hardy estimates of stresses at the atomic sites to determine a spatial description of the stress field. In both estimates, it is found that the crack tip has the highest stress intensity and the remainder of the material ahead of the crack tip experiences rough stress profiles, highlighting the amorphous character of the domain. Behind the crack tip the domain has much lower stress due to the presence of the traction-free surfaces and associated relaxation of the elastic field. The bonds surrounding the rupture location undergo nonlinear elastic deformation involving continuous breaking at the intersection of tetrahedral units.

At the continuum scale, the mathematical expression for the stress field at the crack tip in linearly elastic material is known to follow the following form [89]:

$$\sigma_{yy}(r, \theta) = \frac{K_I}{\sqrt{2\pi r}} \cos\frac{\theta}{2}\left(1 + \sin\frac{\theta}{2}\sin\frac{3\theta}{2}\right), \quad (7)$$

where θ is the angle of a spatial point relative to the projected crack propagation direction. Fitting the stress field data points of aSiO$_2$ by a surface described by the following equation:

$$\sigma_{yy}(r, \theta) = \frac{K_{ic}}{(2\pi r)^\beta} \cos\frac{\theta}{2}\left(1 + \sin\frac{\theta}{2}\sin\frac{3\theta}{2}\right) + c_\infty, \quad (8)$$

we find the exponent $\beta = 1.0$ (with a 95% confidence level of the fit) for each of the stress-estimates. Here, $c_\infty = \sigma_{yy}(\infty, \theta)$ is the uniform normal stress far from the crack tip). This observation highlights that the stress field at the crack tip is highly localized and it decreases much more rapidly from the crack tip compared to what is obtained from the analytical solution. We attribute the sharp decay in stress field as a direct consequence of the stress-fibers that break the long-range character of the elastic field and confine it at the propagating crack front. Next we examine how does a nanopore interacts with the crack tip and affects its propagation in the domain.

To determine the relation between initial crack length a_0 and fracture strength σ_{max}, we conducted continuum scale simulations with the same domain size, loading conditions, and material properties using the finite element software named ABAQUS [90]. The constitutive law obtained from our MD-ReaxFF stress-strain data is used as input to the continuum scale simulations, and the MD stress-strain curve obtained with 10-nm crack was used to fit the FEM stress-strain curve. The goal of this study was to check $\sigma_{max} - a_0$ correlation in MD versus FEM calculations. The strength values obtained from the FE simulations for different a_0 are plotted in Fig. 17, and the data points are well fitted to a nonlinear equation of the form $C_1 + C_2 a_0^n$, where the fitting parameters are $C_2 = 14.25$, $n = -0.482$, and $C_1 = 2.19$ with a R^2 value of 0.997 as the goodness of the fit. As expected the continuum simulation reproduced the exponent to be very close to -0.5 (the small difference comes from finite size effect or the empirical factor a_0/w). The atomistic results on the other hand shows the fitting parameters to be $C_1 = 2.07$, $C_2 = 25.68$, and $n = -0.73$, indicating sharper decay of the fracture strength with a_0. Different sensitivity of the
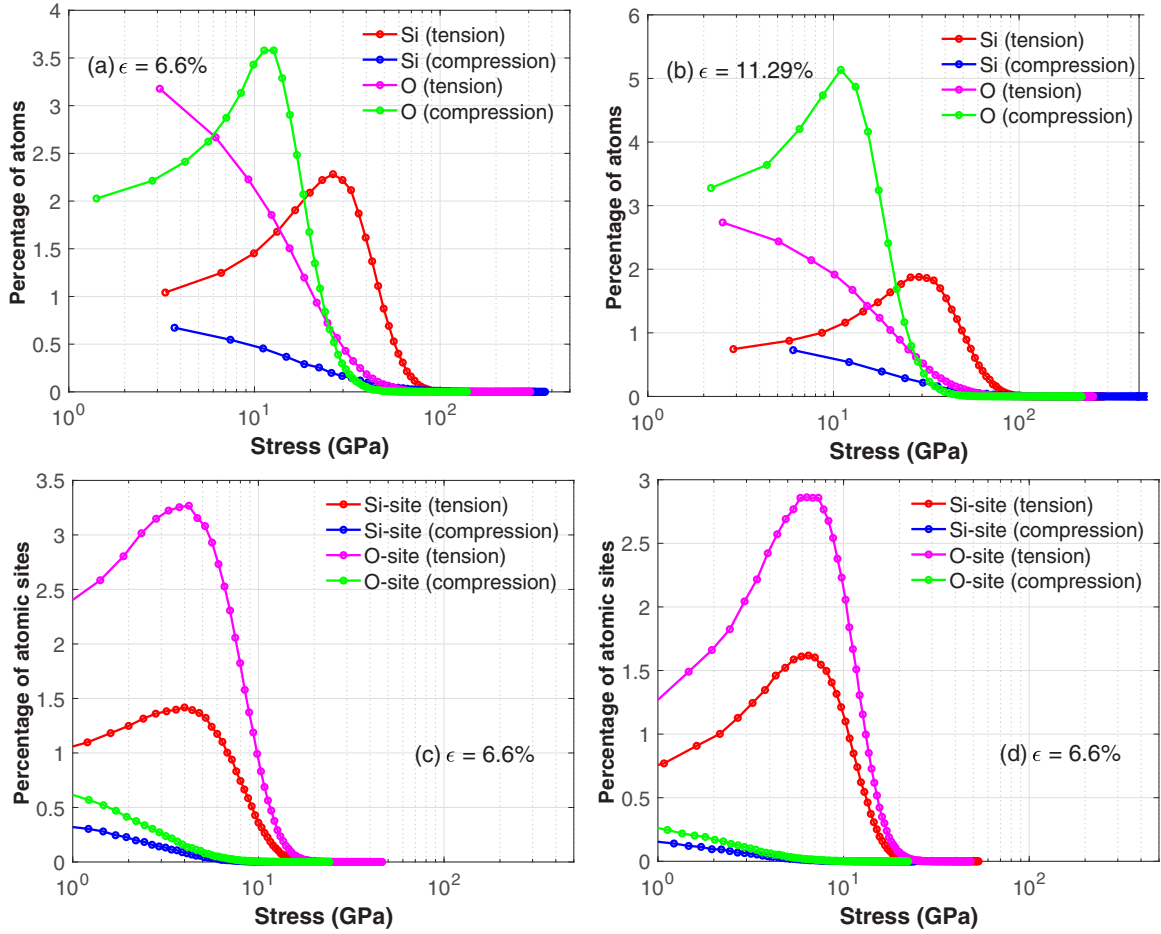
FIG. 15. (Top) Species-dependent virial stress distribution at (a) $\epsilon_{yy} = 0.06660$ during stage A and (b) $\epsilon_{yy} = 0.11290$ during stage-B. (Bottom) Species-dependent Hardy stress distribution at (a) $\epsilon_{yy} = 0.06660$ during stage A and (b) $\epsilon_{yy} = 0.11290$ during stage B.

relation between $\sigma_{\max}$ and a_0 motivates determination of K_{IC} from a second approach.

To obtain a second measure of K_{IC}, we used the formula: $K_{\mathrm{IC}} = \sqrt{G_c E}$, which relates the critical stress-intensity factor K_{IC} with the critical energy release rate G_c. We calculate G_c for our atomistic domain by using the Rice's J integral [44], which is defined as

$$J = \int_{\Gamma} \left(W dy - \mathbf{T} \cdot \frac{\partial \mathbf{u}}{\partial x} ds \right), \tag{9}$$

where $W = \sigma_{ij}\epsilon_{ij}/2$ is the elastic energy density and $\mathbf{T}$ is the traction vector and Γ is the contour enclosing the crack tip. For uniform remote loading along the y direction and the initial crack aligned along the x direction, in finite domains (wherein the contour behind the crack tip is not sufficiently far), the equation for the J integral reduces to $J = \int_{\Gamma_{\mathrm{right}}} W dy + \int_{\Gamma_{\mathrm{left}}} W dy$, where the elastic energy density is written as $W = \sigma_{ij}^{\mathrm{Hardy}} \epsilon_{ij}$. We perform the integration along the contour identified in the inset of Fig. 18, showing the evolution of the J integral for different values of R_c (used to obtain Hardy stresses at the atomic sites) as a function of applied loading.

It is seen that a converged value of $J_{\max} = 7.21$ J m^{-2} results from $R_c > 5.0$ Å (which is consistent with our previous

RDF-based estimation). The stress-intensity factor is thus: $K_{\mathrm{IC}} = \sqrt{E J_{\max} \times 1.0 \times 10^{-3}} = 0.70$ MPa$\sqrt{\mathrm{m}}$, where E is in GPa and J in N m^{-2}. Compared to the fracture-strength-based estimation of K_{IC} the J-integral-based estimation is much closer to the experimental value. Since the J integral is path independent and converged for the domain under consideration, the influence of the finite size effect on J can be considered negligible. Although the relation $K_{\mathrm{IC}} = \sqrt{J_{\max} E}$ relies on the approximation that crack tip stress field decays as $1/\sqrt{r}$, the measure of fracture toughness may not be affected much by the finite size effect of the domain (as long as the J integral is converged, as is the case for the present study). It is thus reasonable to conclude that the J-integral-based estimation of K_{IC} offers a better estimate of fracture toughness, and the Hardy measure of stress plays a crucial role for obtaining the J integral from the virial stresses of the atoms.

2. Crack propagation in porous silica

Porosity in silica is inevitable and it is critical to determine its implication on mechanical properties for understanding the mechanisms of crack propagation and its interaction with porosity. Typical size of nanopores in silica is reported to vary from 1 to 20 nm [83,91]. As the size of the pore increases, the minimum domain size required for modeling an isolated
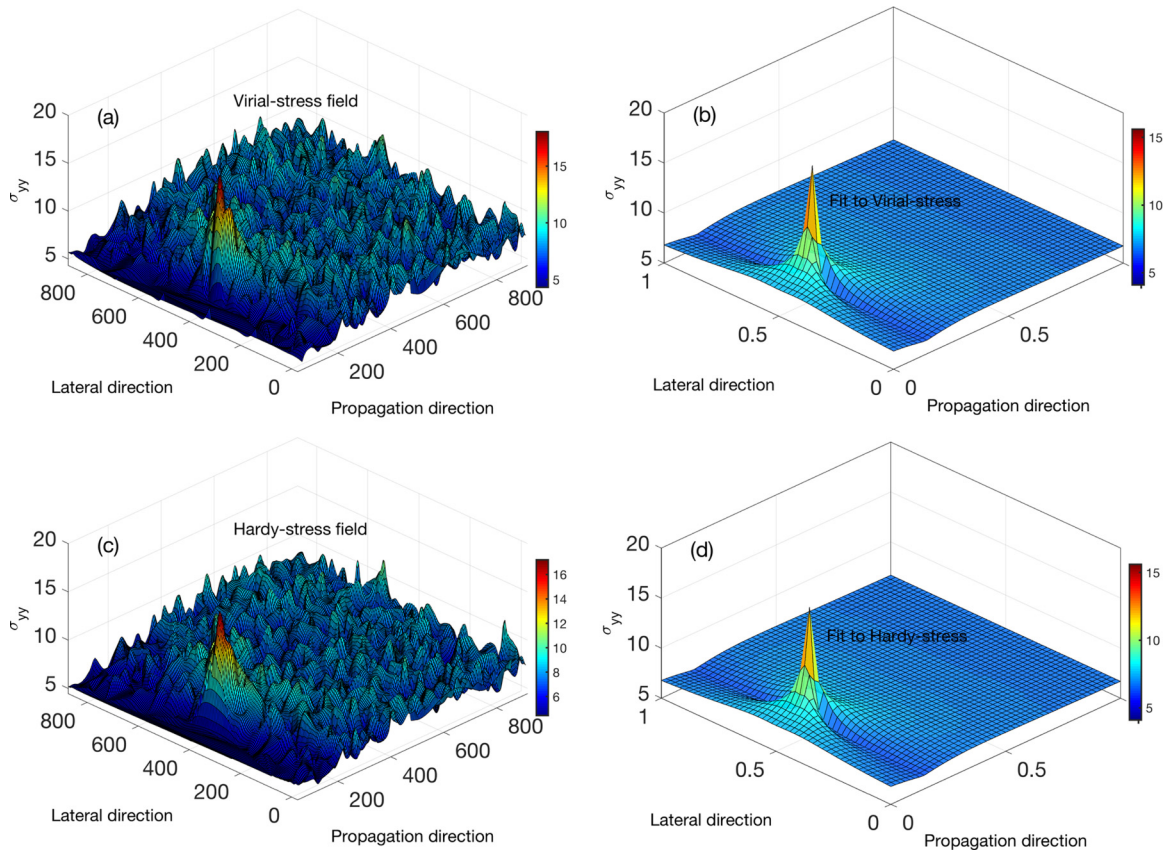
FIG. 16. (a) Spatial variation of the average virial stress field $\sigma_{yy}(r, \theta)$ surrounding the crack tip at the onset of crack propagation. (b) Analytical stress function fitted through the virial stress fields with a R^2 measure of 0.96 as the goodness of fit. The lengths are normalized by the respective dimensions of the domain. (c) Spatial variation of the average Hardy stress field $\sigma_{yy}(r, \theta)$ surrounding the crack tip at the onset of crack propagation. (d) Analytical stress function fitted through the Hardy stress fields with a R^2 measure of 0.97 as the goodness of fit.

pore-crack interaction increases dramatically, making the investigation unfeasible due to large computational requirements. Thus we limit our study to a smaller size range that

vary from 1.07–2.55 nm, and we focus on understanding the effects of single pore on the elastic fields emanating from the crack tip and ascertaining its implication on the criteria for crack propagation. The length of the crack (denoted by a_0) is kept fixed at 100 Å. The distance from the crack tip
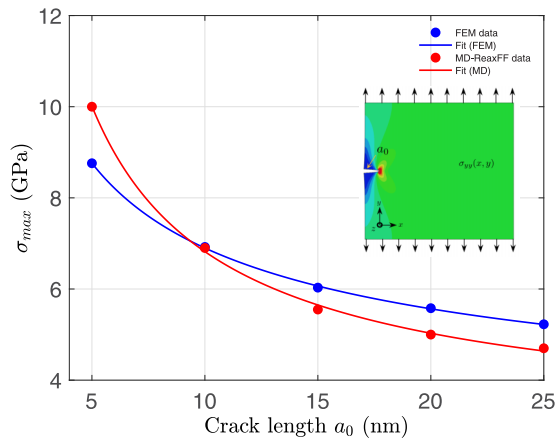
FIG. 17. Variation of strength as a function of crack length in the domain. The blue data point represents the MD-ReaxFF data and the remaining data points are obtained from finite element method simulations of the same domain with its constitutive relation and the cohesive energy being equal to the integrated area of the stress-strain curves obtained from the MD-ReaxFF simulation.
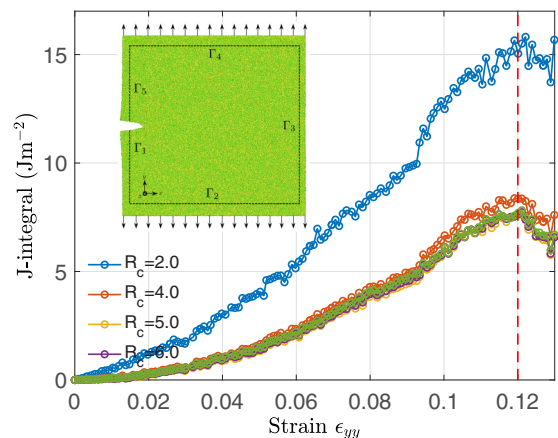
FIG. 18. J integral as a function of applied strain ϵ_{yy} for different values of R_c, which denotes the volume surrounding each atom over which averaging of the virial stress is performed to obtain a Hardy estimate of atomic stress.
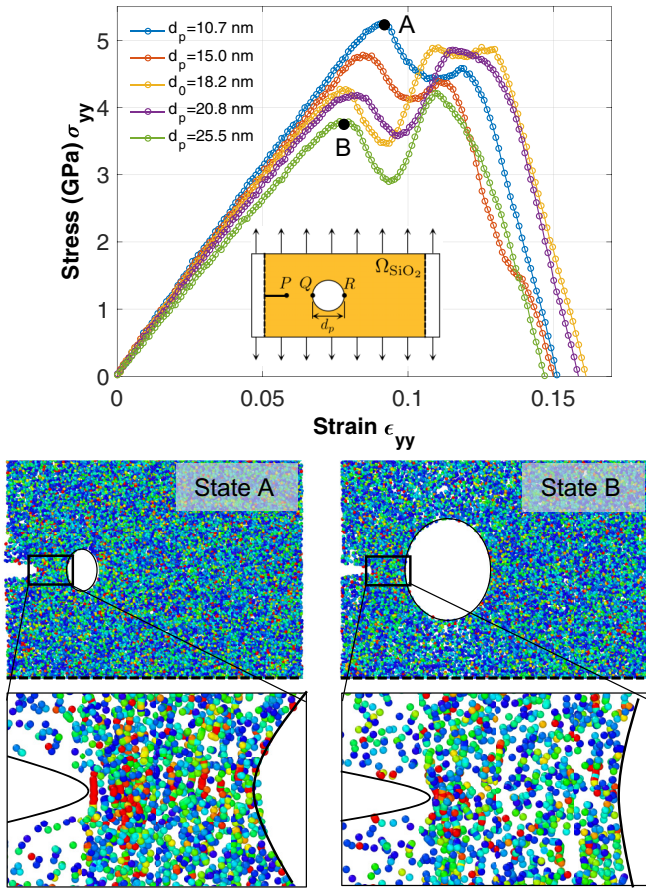
FIG. 19. Effect of pore size $d_p = QR$ (defined in the inset schematic) on stress-strain behavior of porous silica containing one pore of diameter $d_p = 10.7$, 15.0, 18.2, 20.8, or 25.5 nm and an initial crack of length $a_0 = 10$ nm. The distance between the crack tip P and the nearest pore-wall Q is kept at $\lambda = 10$ nm. The figures on the bottom panel showing the stress-fiber pattern at the crack tip at the onset of crack propagation highlights the difference in stress-fiber densities between states A and B and their heterogeneous character.

to the pore wall (denoted here as λ) and the diameter of the pore (denoted by d_p) are varied separately, to determine their relative effects on the atomistic mechanisms that govern the propagation criteria. It has been reported [91] in an array of voids under dilatation to form voids from their edges and coalescence of voids that ultimately lead to failure of the domain. Here we focus on the interaction of a single void with a propagating crack under mode-I loading condition.

At $\lambda = 1.0$ nm, a variation in size of the pore diameter from 1.07 to 2.55 nm (representing 1% to 7% volume fraction of the silica domain), indicates an inverse relationship between the effective stiffness and the pore diameter. As illustrated in Fig. 19(a), the domain with larger d_p shows smaller stiffness. Also, the strength of the domain reduces with increased pore diameter.

From a continuum scale analysis of the stress fields surrounding an isolated hole in an infinite plate under uniaxial tension σ_∞, the maximum stress at the hole edge can be computed analytically from $\sigma_{max} = \frac{W\sigma_\infty}{(W-d)} f(\frac{d}{W})$; where d is the hole diameter; w is the domain width; and $f(\frac{d}{W})$ is

a dimensional stress-intensity factor expressed as $f(\frac{d}{W}) = (3 - 3.14 d/W + 3.667 d^2/W^2)$, which is an empirical law obtained from a continuum scale stress-analysis of a circular hole in a finite plate [92,93]. The ratio d/W in our calculation varies from 0.11 to 0.27. For our domain with a hole of radius $a = 10$ nm and width of $W = 96$ nm, application of the continuum scale formula yields the maximum stress σ_{max} to be 2.97 times higher than the stress on the symmetry plane far from the hole. For a hole diameter of 25 nm, the maximum stress σ_{max} is 3.36 times higher than the macroscopic stress. Thus, from the continuum analysis, the strength of the domain with the smallest pore considered is 13% higher than the domain with the largest diameter pore. However, our atomistic data shows that the domain with the smallest pore is around 40% than stronger that the domain with the largest pore. The effect of pore size is therefore much more pronounced at the atomic scale that what is predicted from the continuum scale formulations. The difference can be attributed to the amorphous character of the lattice, formation of stress-fibers, and localized atomistic information (such as bond coordination, crystal structure) which are not taken into account in the continuum scale analysis. It is thus important to explore the atomistic information to correctly ascertain the effect of nanopores on the effective properties of a porous complex media such as amorphous silica.

Furthermore results show that there are two stress peaks in the stress-strain data: the first peak (denoted here by σ_{max-1}) corresponds to the maximum macroscopic stress at the onset of the crack propagation, and the second peak (denoted here by σ_{max-2}) corresponds to the maximum macroscopic stress at the onset of crack re-nucleation at the pore wall on the right hand side of the pore. The first peak stress decreases with pore size, while the second stress peak does not show any specific trend except that it is smaller than the first peak stress for sufficiently larger pores. Reduction of the maximum macroscopic stress with larger pores indicates the influence of the pore on the crack-propagation criteria: the larger the pore size is, the higher is the average stress on the symmetry plane. As a result, for a given volume of the material, with larger pores the crack tip reaches its local bond breaking stress earlier compared to the smaller pores. Also, at a given macroscopic strain, the stress field of the pores interact with the stress field emanating from the crack tip affecting the criteria for crack propagation. The overall maximum macroscopic stress is thus higher for the smaller pores due to crack-pore interaction.

Similar to the effective strength of the domain, the effective toughness is also substantially affected by the presence of the pore. To compute toughness of the domain, we resort to the energy based definition of toughness and evaluate it through integrating the area under the stress-strain curve: $\int_0^{\epsilon_f} \sigma \, d\epsilon$, where ϵ_f is the fracture strain. Results show no clear correlation between effective toughness and pore size. As the pore size increases from 1.0 to 1.5 nm, the effective toughness gradually goes down. For a 20-nm pore, it goes up; and for a 25 nm pore, it reduces again. Such behavior can be attributed to the complex interplay between the stress fields of the pore and the crack tip; the distance between the crack tip and the pore wall; and the curvature of the pore, which affects the criteria for renucleation of the secondary crack at other end
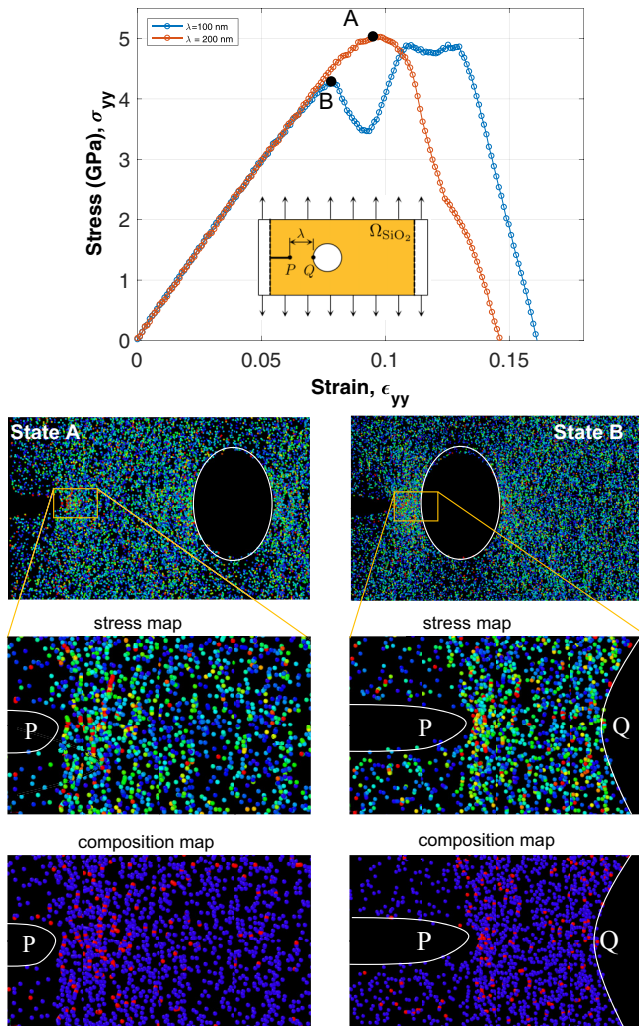
FIG. 20. Effect of λ (defined in the inset schematic in the top figure) on the stress-strain behavior of the porous domain. The initial crack length is $a_0 = 10$ nm and the distance between the crack tip and the pore wall is $\lambda = 10$ nm.

of the pore. With much higher pore size, however, the criteria for crack renucleation can be deemed to converge to a single value as $d_p \to \infty$.

Moreover for a given pore size, variation in distance between the pore wall and the crack tip (denoted here by λ) shows substantial effects on effective strength and toughness of the domain. Figure 20 compares two situations wherein $\lambda = 10$ and 20 nm. The stress-strain curve shows only one peak when $\lambda = 20$ nm, which is similar to what we have seen for the domain with a crack but no pore. On the other hand, the stress-strain curve for $\lambda = 10$ nm shows two peaks with much higher toughness. The strength of the domain remains the similar but there is a sizable difference in terms of their strength. The behavior of domain with $\lambda = 20$ nm suggests that for a sufficiently large distance between the crack tip and the pore the stress field of the crack tip is unaffected by the presence of the pore. Yet the domain exhibits only one peak in its strain curve. We propose that this happens for the following reason. By the time the crack tip reaches point Q upon satisfying the local fracture criteria at point P, the edge

on the other side of the pore obtains sufficiently large elastic strain energy so that renucleation happens at that edge without requiring any additional energy. Continued propagation of the crack is thus energetically favorable. On the other hand, for smaller choice of λ, the edge R does not reach at its renucleation energy level when the crack arrives at point Q. With continued loading, macroscopic stress thus continues to increase giving rise to a second peak. The simulations were conducted with a maximum domain width of 95 nm along the crack-propagation direction which gives the ratio between the crack length and the domain width as 0.1. Thus we consider the width to be sufficiently large to assume the factors involving λ/w (appearing in the equations for the stress-intensity factors) as negligible. Yet is obvious that propagation of crack in porous silica is affected by the interacting elastic fields—and the stress-fibers play an important role in modulating the elastic fields.

IV. CONCLUDING REMARKS

To conclude, we have demonstrated several important atomic scale features of crack nucleation and propagation in amorphous silica using the virial stress fields. First, we show that virial stress structure is highly heterogeneous in silica, and its species-dependent structure shows the Si and O atoms to play distinctive roles in carrying the macroscopic load. From the virial stress structure it is found that the Si atoms are the majority tensile stress carriers, whereas the O atoms are the compressive stress carriers. Second, localized rupture starts much earlier than what is noticeable from the macroscopic stress-strain data. Third, at the crack nucleation site or the propagating front of an initial crack tip exhibits formation of virial stress-fibers of finite length which upon reaching a critical density triggers the crack nucleation and propagation processes in silica. The formation of the virial stress-fibers and atomic rearrangement and reorientation offer resistance for propagation of bond rupturing surrounding the nucleating site or propagating crack tip. The strength and toughness of the domain with and without crack and with and without a pore unambiguously depict a clear virial stress structure that can be exploited to explain the atomistic processes governing fracture. The density of stress-fibers intensifies at the crack tip when it interacts with the elastic fields of a neighboring pore. Fourth, the crack-tip stress field vary as $1/r$ from the crack tip. Formation of nano stress-fibers localizes the stress fields at the evolving crack front and limits its long-range elastic tail into the far-field domain. And fifth, presence of nanopores within an interaction distance of 20 nm substantially improves the effective toughness of the domain. Overall, the results unambiguously demonstrate strong heterogeneous character of the amorphous material and the distinctive roles of the individual species that make it behave very differently from what is seen in homogeneous and crystalline materials. We also show that virial stress structure can be used to examine the atomic scale features governing nucleation and propagation events from the atomic scale, while the Hardy stress fields provide robust framework to examine continuum scale quantities such as fracture toughness.

It is expected that the fundamental understanding outlined in this paper will find critical applications in exploring

pathways for controlling crack nucleation and propagation by promoting the formation the stress-fibers and engineering their mechanical behavior by incorporating doping or alloying with a different species. Also, we believe the results and discussions presented here would create a new dimension to our understanding fracture in important class of amorphous materials such as silica. By assessing the behavior of the individual species and their load carrying capability at different states of mechanical loading, a new class of materials could be produced. It is also expected that this work would promote development of new theories that can capture the rapid decay in elastic field and yet construct a robust framework for calculating effective toughness and strength of amorphous solids.

[1] A. Schiffrin, T. Paasch-Colberg, N. Karpowicz, V. Apalkov, D. Gerster, S. Mühlbrandt, M. Korbman, J. Reichert, M. Schultze, S. Holzner *et al.*, Nature (London) **493**, 70 (2013).

[2] M. Ferrera, L. Razzari, D. Duchesne, R. Morandotti, Z. Yang, M. Liscidini, J. Sipe, S. Chu, B. Little, and D. Moss, Nat. Photon. **2**, 737 (2008).

[3] L. Tong, R. R. Gattass, J. B. Ashcom, S. He, J. Lou, M. Shen, I. Maxwell, and E. Mazur, Nature (London) **426**, 816 (2003).

[4] D. S. Brauer, Angew. Chem., Int. Ed. Engl. **54**, 4160 (2015).

[5] G. Brambilla and D. N. Payne, Nano Lett. **9**, 831 (2009).

[6] H. Nsubuga, C. Basheer, M. B. Haider, and R. Bakdash, J. Chromatogr., A **1554**, 16 (2018).

[7] A. Rahikkala, J. M. Rosenholm, and H. A. Santos, in *Biomedical Applications of Functionalized Nanomaterials* (Elsevier, UK, 2018), pp. 489–520.

[8] Z. H. Stachurski, *Fundamentals of Amorphous Solids: Structure and Properties* (Wiley, Germany, 2015).

[9] L. Wondraczek, J. C. Mauro, J. Eckert, U. Kühn, J. Horbach, J. Deubener, and T. Rouxel, Adv. Mater. **23**, 4578 (2011).

[10] B. Guillot and Y. Guissani, Phys. Rev. Lett. **78**, 2401 (1997).

[11] C. L. Rountree, D. Vandembroucq, M. Talamali, E. Bouchaud, and S. Roux, Phys. Rev. Lett. **102**, 195501 (2009).

[12] J. Rimsza and J. Du, npj Mater. Degrad. **2**, 18 (2018).

[13] F. Leonforte, A. Tanguy, J. P. Wittmer, and J.-L. Barrat, Phys. Rev. Lett. **97**, 055501 (2006).

[14] S. T. Bromley, M. A. Zwijnenburg, and T. Maschmeyer, Phys. Rev. Lett. **90**, 035502 (2003).

[15] K. Geirhos, P. Lunkenheimer, and A. Loidl, Phys. Rev. Lett. **120**, 085705 (2018).

[16] S. J. Tracy, S. J. Turneaure, and T. S. Duffy, Phys. Rev. Lett. **120**, 135702 (2018).

[17] G. Pezzotti and A. Leto, Phys. Rev. Lett. **103**, 175501 (2009).

[18] S. J. Turneaure, S. M. Sharma, and Y. M. Gupta, Phys. Rev. Lett. **121**, 135701 (2018).

[19] F. Yuan and L. Huang, J. Non-Cryst. Solids **358**, 3481 (2012).

[20] C. Meade and R. Jeanloz, Science **241**, 1072 (1988).

[21] C. Meade, R. J. Hemley, and H. K. Mao, Phys. Rev. Lett. **69**, 1387 (1992).

[22] X. Bidault, S. Chaussedent, W. Blanc, and D. R. Neuville, J. Non-Cryst. Solids **433**, 38 (2016).

[23] N. M. Anoop Krishnan, B. Wang, Y. Yu, Y. Le Pape, G. Sant, and M. Bauchy, Phys. Rev. X **7**, 031019 (2017).

[24] Y. Yu, N. A. Krishnan, M. M. Smedskjaer, G. Sant, and M. Bauchy, J. Chem. Phys. **148**, 074503 (2018).

[25] N. A. Krishnan, B. Wang, Y. Le Pape, G. Sant, and M. Bauchy, Phys. Rev. Materials **1**, 053405 (2017).

[26] A. Debelle, J.-P. Crocombette, A. Boulle, A. Chartier, T. Jourdan, S. Pellegrino, D. Bachiller-Perea, D. Carpentier, J. Channagiri, T.-H. Nguyen *et al.*, Phys. Rev. Mater. **2**, 013604 (2018).

[27] T. Du, H. Li, G. Sant, and M. Bauchy, J. Chem. Phys. **148**, 234504 (2018).

[28] Y. Yu, B. Wang, M. Wang, G. Sant, and M. Bauchy, J. Non-Cryst. Solids **443**, 148 (2016).

[29] F. Ebrahem and B. Markert, PAMM **17**, 235 (2017).

[30] K. Muralidharan, J. Simmons, P. Deymier, and K. Runge, J. Non-Cryst. Solids **351**, 1532 (2005).

[31] A. Pedone, G. Malavasi, M. C. Menziani, U. Segre, and A. N. Cormack, Chem. Mater. **20**, 4356 (2008).

[32] R. Ochoa, T. P. Swiler, and J. H. Simmons, J. Non-Cryst. Solids **128**, 57 (1991).

[33] T. P. Swiler, J. H. Simmons, and A. C. Wright, J. Non-Cryst. Solids **182**, 68 (1995).

[34] P. K. Gupta and C. R. Kurkjian, J. Non-Cryst. Solids **351**, 2324 (2005).

[35] N. P. Bansal and R. H. Doremus, *Handbook of Glass Properties* (Elsevier, New York, 2013).

[36] F. T. Wallenberger, J. C. Watson, and H. Li, Materials Park, OH: ASM International, 2001 (2001), pp. 27–34.

[37] S. M. Wiederhorn, J. Am. Ceram. Soc. **52**, 99 (1969).

[38] B. Proctor, I. Whitney, and J. Johnson, Proc. R. Soc. London A **297**, 534 (1967).

[39] S. C. Chowdhury, B. Z. G. Haque, and J. W. Gillespie, J. Mater. Sci. **51**, 10139 (2016).

[40] F. Ebrahem, F. Bamer, and B. Markert, Comput. Mater. Sci. **149**, 162 (2018).

[41] J. M. D. Lane, Phys. Rev. E **92**, 012320 (2015).

[42] T. Hao, Ph.D. thesis, University of Delaware, 2018.

[43] B. Wang, Y. Yu, M. Wang, J. C. Mauro, and M. Bauchy, Phys. Rev. B **93**, 064202 (2016).

[44] J. R. Rice, J. Appl. Mech. **35**, 379 (1968).

[45] G. R. Irwin, SPIE Milestone Ser. **137**, 167 (1997).

[46] A. A. Griffith, Philos. Trans. R. Soc. London, Ser. A, 163 (1921).

[47] M. Z. Hossain, T. Ahmed, B. Silverman, M. S. Khawaja, J. Calderon, A. Rutten, and S. Tse, J. Mech. Phys. Solids **110**, 118 (2018).

[48] A. R. Zak and M. L. Williams (California Institute of Technology, 1962).

[49] T. Cook and F. Erdogan, Int. J. Eng. Sci. **10**, 677 (1972).

[50] F. Erdogan and V. Biricikoglu, Int. J. Eng. Sci. **11**, 745 (1973).

[51] C. Atkinson and J. Eshelby, Int. J. Fract. Mech. **4**, 3 (1968).

[52] C. Atkinson, Int. J. Eng. Sci. **13**, 489 (1975).

[53] H. Ming-Yuan and J. W. Hutchinson, Int. J. Solids Struct. **25**, 1053 (1989).

[54] M.-Y. He and J. W. Hutchinson, J. Appl. Mech. **56**, 270 (1989).

[55] K. Vollmayr, W. Kob, and K. Binder, Phys. Rev. B **54**, 15808 (1996).

[56] A. C. Van Duin, A. Strachan, S. Stewman, Q. Zhang, X. Xu, and W. A. Goddard, J. Phys. Chem. A **107**, 3803 (2003).

[57] J. C. Fogarty, H. M. Aktulga, A. Y. Grama, A. C. Van Duin, and S. A. Pandit, J. Chem. Phys. **132**, 174704 (2010).

[58] M. A. Qomi, K. Krakowiak, M. Bauchy, K. Stewart, R. Shahsavari, D. Jagannathan, D. B. Brommer, A. Baronnet, M. J. Buehler, S. Yip *et al.*, Nat. Commun. **5**, 4960 (2014).

[59] M. Bauchy, M. J. A. Qomi, C. Bichara, F.-J. Ulm, and R. J.-M. Pellenq, Phys. Rev. Lett. **114**, 125502 (2015).

[60] J. M. Rimsza, R. E. Jones, and L. J. Criscenti, J. Am. Ceram. Soc. **101**, 1488 (2018).

[61] S. Plimpton, J. Comput. Phys. **117**, 1 (1995).

[62] A. Pedone, G. Malavasi, A. N. Cormack, U. Segre, and M. C. Menziani, Chem. Mater. **19**, 3144 (2007).

[63] M. Bauchy, J. Chem. Phys. **141**, 024507 (2014).

[64] K. Muralidharan, K.-D. Oh, P. A. Deymier, K. Runge, and J. Simmons, J. Mater. Sci. **42**, 4159 (2007).

[65] O. V. Mazurin, M. V. Streltsina, and T. P. Shvaiko-Shvaikovskaya, (Elsevier, 1983), xv+ 669, 1983 (1983).

[66] Y. Yu, M. Wang, M. M. Smedskjaer, J. C. Mauro, G. Sant, and M. Bauchy, Phys. Rev. Lett. **119**, 095501 (2017).

[67] C. R. Kurkjian, P. Gupta, R. K. Brow, and N. Lower, J. Non-Cryst. Solids **316**, 114 (2003).

[68] G. Marc and W. G. McMillan, Adv. Chem. Phys. **58**, 209 (1985).

[69] A. K. Subramaniyan and C. Sun, Int. J. Solids Struct. **45**, 4340 (2008).

[70] J. G. Kirkwood and F. P. Buff, J. Chem. Phys. **17**, 338 (1949).

[71] J. Irving and J. G. Kirkwood, J. Chem. Phys. **18**, 817 (1950).

[72] R. J. Hardy, J. Chem. Phys. **76**, 622 (1982).

[73] R. J. Hardy, J. Chem. Phys. **145**, 204103 (2016).

[74] Y. Chen and A. Diaz, Phys. Rev. E **98**, 052113 (2018).

[75] A. Torres-Sánchez, J. M. Vanegas, and M. Arroyo, Phys. Rev. Lett. **114**, 258102 (2015).

[76] T. Delph, Proc. R. Soc. London A **461**, 1869 (2005).

[77] Z. Fan, L. F. C. Pereira, H.-Q. Wang, J.-C. Zheng, D. Donadio, and A. Harju, Phys. Rev. B **92**, 094301 (2015).

[78] D. Tsai, J. Chem. Phys. **70**, 1375 (1979).

[79] M. Zhou, Proc. R. Soc. London, Ser. A **459**, 2347 (2003).

[80] J. A. Zimmerman, E. B. WebbIII, J. Hoyt, R. E. Jones, P. Klein, and D. J. Bammann, Modell. Simul. Mater. Sci. Eng. **12**, S319 (2004).

[81] A. Diaz, D. Davydov, and Y. Chen, Proc. R. Soc. London A **475**, 20180688 (2019).

[82] M. Bauchy, B. Wang, M. Wang, Y. Yu, M. J. A. Qomi, M. M. Smedskjaer, C. Bichara, F.-J. Ulm, and R. Pellenq, Acta Mater. **121**, 234 (2016).

[83] C. Rountree, S. Prades, D. Bonamy, E. Bouchaud, R. Kalia, and C. Guillot, J. Alloys Compd. **434**, 60 (2007).

[84] M. Wang, B. Wang, T. K. Bechgaard, J. C. Mauro, S. J. Rzoska, M. Bockowski, M. M. Smedskjaer, and M. Bauchy, J. Non-Cryst. Solids **454**, 46 (2016).

[85] S. Kapoor, K. Januchta, R. E. Youngman, X. Guo, J. C. Mauro, M. Bauchy, S. J. Rzoska, M. Bockowski, L. R. Jensen, and M. M. Smedskjaer, Phys. Rev. Mater. **2**, 063603 (2018).

[86] M. Liu, Y. Gan, D. A. Hanaor, B. Liu, and C. Chen, Eng. Fract. Mech. **149**, 134 (2015).

[87] V. Hatty, H. Kahn, and A. H. Heuer, J. Microelectromech. Syst. **17**, 943 (2008).

[88] A. T. Zehnder, Available for public use at Cornell University website http://ecommons.library.cornell.edu/bitstream/1813/3075/6/fracture_notes_2008.pdf (2007).

[89] G. C. Sih, Int. J. Fract. Mech. **2**, 628 (1966).

[90] D. Systemes, Dassault Systemes: Paris, France (2019).

[91] Y.-C. Chen, Z. Lu, K.-i. Nomura, W. Wang, R. K. Kalia, A. Nakano, and P. Vashishta, Phys. Rev. Lett. **99**, 155506 (2007).

[92] A. F. Grandt, Int. J. Fract. **11**, 283 (1975).

[93] M. Mohammadi, J. R. Dryden, and L. Jiang, Int. J. Solids Struct. **48**, 483 (2011).